UNIVERSITAT POLITÈCNICA DE CATALUNYA
BARCELONATECH

Departament de Teoria del Senyal
i Comunicacions

Master of Science Thesis

Characterization of Errors and Noises in MEMS Inertial Sensors Using Allan Variance Method

by

Leslie Barreda Pupo

Supervisors: Josep Maria Mirats Tur,
Maria Concepcion Santos Blanco

Barcelona, 2016

To my beloved husband for his support, to my mother for be there for me.

Contents

Acknowledgements

I would like to thank my supervisors Josep Maria Mirats Tur and Maria Concepcion Santos Blanco for their continuous support, encouragement, guidance and advice during the Master period. I also would like to express my sincere gratitude to Diego Garcia for his contributions, kind assistance and friendship.

Chapter 1

Introduction

1.1 Motivation

Navigation systems have an important role in the history of mankind and will continue to do so in the future. They are required to provide information of a position of a moving object with respect to a well known reference frame. Several forms of navigation have been used since long time ago. Travellers used to follow a map and determine his position by observing roads, rivers, mountains, etc. Navigators used to determine his position by stablishing a fixed star as a reference frame, usually referred to as inertial reference frame [1].

From the basic ways of traveling until modern unmanned vehicles, the navigation systems may be clasified as: *pilotage*, where the navigator identifies landmarks and infers from these the position and the orientation; *dead reckoning*, where the navigator knows the vessel initial position and orientation, and the estimated position and orientation is thereafter inferred from the motion of the vessel, i.e. heading and speed; *celestial navigation*, which relies on the navigator ability to use known celestial objects (e.g. sun, moon, planets, stars) and knowledge of the movements of the Earth to estimate the current position and orientation; *radio navigation*, which relies on radio frequency sources with known locations (e.g. global navigation satellite systems or radio beacons); *inertial navigation*, which relies on the navigator to know the vessel initial position, velocity and attitude, and inferring the estimated position and orientation from measuring the linear acceleration and angular velocity of the system, estimating the position relative to the initial point.

In the modern days, Inertial Navigation Systems (INS) have an increasing wide range of applications covering navigation of cars, ships, aircrafts, spacecrafts,etc [2]. INS have also applications in the militar industry as can be tactical and strategic missiles. There are also applications in the field of robotics and in the survey of underground pipelines [3]. Different methods and technologies have been developed, improved and evolved, enabling increasing levels of accuracy in their measurements [1]. Eventhougth the basic principles of INS do not change from one application to another, the accuracy of the inertial sensors and the precision of the associated computation that should be carried out, varies dramatically over the range of applications [4].

The operation of INS are based in the classical mechanical laws of Newton, who established that a moving object will have an acceleration if an external force is applyed over it, changing its uniform straight movement. Measuring this acceleration, doing some mathematical operations, it is possible to obtain the velocity and position of the object. The device capable of measure the acceleration is known as accelerometer [5].

Among other components, an INS have three acceleremoters which measure the acceleration in a single direction, each one measuring in one axis, and three gyroscopes which measure the deviation of the direcction pointed by the accelerometers, sensing the rotational motion of a body respect the orientation of accelerometers at all times [6] [7].

When the three accelerometers and gyroscopes are used to determine the position, this process is calle inertial navigation, and the unit where all these sensors are embeeded are called Inertial Measurement Unit (IMU).

IMUs have expanded from their traditional military usage and are now finding wider application in industrial segments. With their more compact form factors, lower power requirements, higher stability, and better accuracy, today's IMUs give designers flexibility when they are creating inertial sensing and control applications. To select the proper IMUs, it's important to understand how their specifications (and error sources) can affect positioning, velocity, and orientation.

An important disadvantage of the inertial sensors are the significant errors which are present in measurements. The IMU measurements are usually corrupted by different types of error sources such as sensor noises, scale factor and bias variations with temperature, etc. By integrating the IMU measurements in the navigation algorithm, these errors will be accumulated, leading to significant drift in the position and velocity outputs. The inertial sensor errors lie in two parts: deterministic and stochastic.

The deterministic part includes error due to the constant bias, axis non orthogonality, axis misalignement, which are removed from measurements by the corresponding calibration techniques. The stochastic part contains random errors, usually called noises, that can not be removed from measurements and should be modeled as stochastic processes. The same error models can be used for inertial navigation and for stabilization applications.

Several methods have been developed to model the stochastic noise of the inertial sensors, as can be the Adaptive Kalman Filter [8] [9], frequency domain approaching using spectral density [10], as well as variance techniques where the most known and used is the Allan Variance method [11] [12] [13].

Once the noises are identified and their values known, to remove the noise effect in the measurements at the post-processing stage of the signal, a noise removal technique is applied [14]. The process of noise removal is generally referred to as signal denoising or simply denoising, where smoothing filters are applied, such as the well known technique named Wavelet denoising [15]. In this way, the position of an IMU can be determined in a more accurate way.

To select the proper IMU for an application, the sensor's parameters to be taken into account for a specific purpose are the accuracy, reliability, repeatability, weigth/size and cost. Once the proper gyro is selected, its error source must be understood and characterized by the development of a suitable error model, and afterwards a signal denoising technique should be applied to obtain the more accurate posible position of a vehicle where the IMU is embeeded.

1.2 Aim of the Thesis

The aim of this work is to develop a simple and effective tool that can be used, in an accurate way, to characterize and quantify the types and values of the noises affecting any gyros and accelerometers that we need to use or compare, depending on the application we want to develop. Hence, once the error and noise parameters are known, they can be used to correct and improve the estimated position.

To have previously identified the errors or noises values on the sensors' outputs will serve us for correcting, or taking into account, in the final obtained position.

For that purpose, in this work several aspects of the inertial sensors will be studied in order to have a complete overview of the existing technologies, the principle of functioning of gyros and accelerometers, advantages and disadvantages and suitability depending on the application, future trends, and so on. More focus will be put on the study of the MEMS technology for its suitability for industrial applications and its good cost/performance relation, as these will be the features needed for the applications we will be developing.

A deeper study will be carried out for the noise and error terms affecting gyroscopes and accelerometers as well as their characterization. From previous and basics findings the Allan Variance method has been identified to be a powerful and straightforward method for error and noise characterization in inertial sensors. Therefore, a deep study of the concepts, methodology, equations of the Allan Variance method will be performed.

A practical implementation of the method using the IMU 3DM-GX3-25 in an experimental setup will serve us to test the Allan variance methodology. For the tests several datasets will be collected. An Allan Variance toolbox will be implemented in the Matlab environment in order to process the data gathered by the sensors, and it will serve as the tool for gyroscopes and accelerometers analysis. After the identification and characterization of the noises terms present in our sensor, a process of denoising will be needed. In that sense, some digital signal filters as the Wavelet Transform and the Median Filter, will be studied. The Discrete Wavelet Transform and the Median Filter will be also implemented in the Matlab code in order to evaluate if the previously detected noises are removed or at least their values are reduced. As a summary, the work will be addressing the following:

- Study of inertial gyroscopes and accelerometers.
- Theorical analysis of the Allan Variance method.
- Practical implementation of the Allan Variance and analysis of the experimental results.

1.3 A Thesis overview

The thesis is organized in the following manner: Chapter 2 deals with the inertial sensors (gyroscopes and acceleremoters), their basic principles, different types and technologies. Also the type of errors inherent to gyros and accelerometers are described.

In Chapter 3, the Allan variance method, that will be used to model the stochastic noise of the experimental inertial sensors, is reviewed and its principles analyzed. The main error sources and noises, involved in inertial sensors measurements, are reviewed. Moreover, denoising techniques, as the Wavelet method and median filtering, are detailed and used to reduce the noise.

Chapter 4 is devoted to the experimental tests carried out to model stochastic noises in an IMU with Allan variance method, and the results obtained are analyzed. Once characterize and sense the errors affecting the experimental sensors, the Wavelet denoising method is applied in order to correct and remove the error components of the signal. Results of the denoising are analyzed.

Finally, in Chapter 5 the conclusions of this work are presented.

Chapter 2

Inertial Sensors: Gyroscopes and Accelerometers

2.1 Introduction

Inertial sensors comprise accelerometers and gyroscopes, commonly abbreviated to gyros. An accelerometer measures specific acceleration and a gyroscope measures angular rate, both without an external reference.

Gyros and accelerometers are key for INS. Historically, gyros have been used in many applications due to their capacity to sense the angle turned and the angular rate of turn over a defined axis of a structure. An earliest convencional gyros consisted in a rotating wheel mounted in two gimbals that can rotate in the three coordinate axes, and related parts able to measure the angle rate changes about the coordinate system.

Recent designs involve sensing mechanisms based in physic phenomena such as vibrating quartz and silicon, optical and micro electro mechanical techniques.

This chapter describes the basic principles of gyros and accelerometer technology, analyzes the different types of sensors, and reviews the error sources. Section 2.2 deals with conventional mechanical sensors outlining the most relevant types. Sections 2.3 and 2.4 deal with optical and micro electro mechanical (MEMS) sensors, respectively, the different types and technologies, and the main highlights of each technology. Section 2.5 gives an overview of the main error sources involved in inertial sensor measurements, their different types, quantification and the overall contribution of each one to the final result. Finally, section 2.6 deals about the current and future trends in the inertial sensor developments.

2.2 Mechanical sensors

2.2.1 Mechanical gyros

Conventional gyros use the inertial properties of a spinning wheel or rotor. In general, mechanical gyros are composed, in its simple way, by a rotor/wheel, gimbals, pick-offs and a spin motor, as shown in Fig. 2.1.

When a mechanical gyro is suffering a rotation, the wheel will be kept in the constant global orientation, due to the conservation of the angular momentum effect, and the angles between

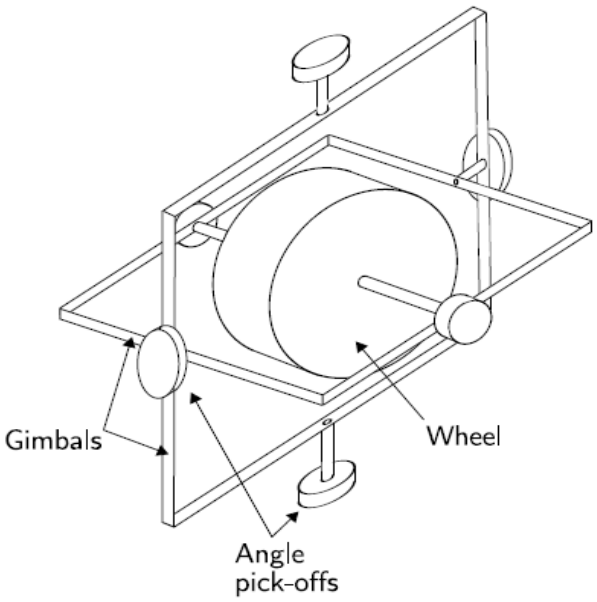

Figure 2.1: A conventional mechanical gyroscope [1].

adjacent gimbals can be read using the angles pick-off [4] [16]. Within the mechanical gyroscope classes, we can find the rate-integrating, the tuned rotor, the flex, the rate, the vibratory, the tuning fork, the quartz, the silicon and the nuclear magnetic resonance sensors. Many of these devices are shown in Fig. 2.2.

Rate-integrating gyros has been used in different applications including navigation systems in aircraft, ships and guided weapons. Unfortunately, this sensor is sensitive to linear and angular accelerations, causing errors in measurements. Temperature changes modify the characteristic of the magnetic materials within the sensors. It was fully developed and used in strapdown systems in many types of vehicles [17].

The tuned rotor gyro have found similar applications as the rate-integrating gyros, and also share the same error sources [18].

The flex gyro operates in similar manner to the tuned rotor gyro, and was developed in the middle of the 1970s. Errors in measurement come from the same sources as the tuned gyro, and have very similar applications [1].

The rate sensors has lower accuracy than the rate-integrating and the tuned rotor gyroscopes accuracies, thus, it is not very useful for navigation applications [7] [19].

Vibratory gyros has a vibrating element has taken different shapes such as string, a rod, a tuning fork, a beam and hemispherical dome. The limitations of vibratory gyros lie in having high drift rates, sensitivity to environmental effects, etc. Within their applications of these gyros, the providing of feedback for stabilisation or angular position measurements, are the most common [20] [21].

The tuning fork sensor has two vibrational elements mounted in parallel on a base. When the structures are excited to vibrate in opposite, the resultant effect is similar to the motion of tuning fork elements [22].

The quartz rate sensor bases its operation in the tuning fork principles, and can have several rate sensitivities. These devices are micromachined and are the cutting edge of MEMS technology [23].

The silicon sensor, as manufactured with silicon material, has a lot of properties which make it

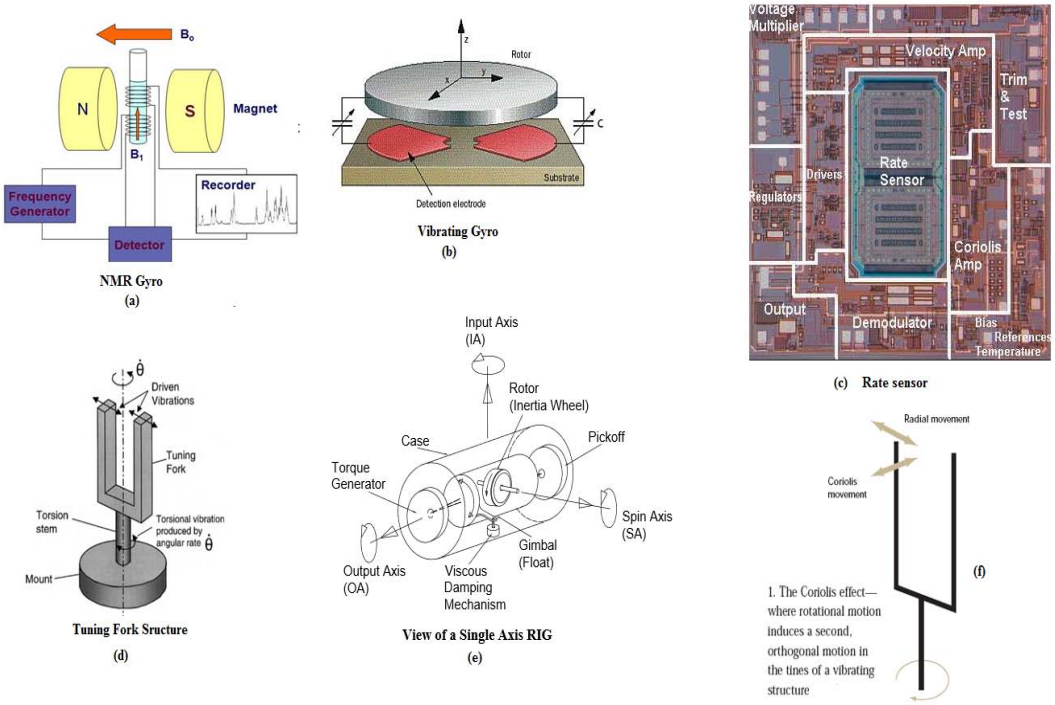

Figure 2.2: Different types of gyroscopes, (a) NMR, (b) Vibrating, (c) Rate, (d) Tuning fork, (e) Rate integrating. (f) The Coriolis effect, which it is a physical phenomena for many gyros.

very suitable for small integrated devices, besides its low cost, and its non-magnetic, good electric and elastic properties [24].

Nuclear magnetic resonance (NMR) does not have moving parts. NMR is a physical effect that comes of the interaction between the nuclei of several elements and the exterior magnetic field. In presence of a magnetic field, the spin nuclei is subject to a torque, resulting in a precession of the nuclei spin axis around the direction of the magnetic field [25] [26].

A more detaild description about characteristics, behaviour and applications of these types of mechanical gyroscopes can be found in literature [1] [7].

The need of high precision in applications lead to the development of gyroscopes based on optical and micro electo mechanical technologies. In sections 2.3 and 2.4 deal with these kind of gyros and their main characteristic and applications.

2.2.2 Mechanical accelerometers

Figure 2.3 shows the operation principle of an acceleremoter. A proof mass is free to move with respect to the accelerometer case along the accelerometers sensitive axis, restrained by springs. A pick-off measures the position of the mass with respect to the case.

When an accelerating force along the sensitive axis is applied to the case, the proof mass will initially continue at its previous velocity, so the case will move with respect to the mass, compressing one spring and stretching the other. Stretching and compressing the springs alters the forces they transmit to the proof mass from the case. Consequently, the case will move with respect to the mass until the acceleration of the mass due to the asymmetric forces exerted by the springs matches the acceleration of the case, due to the externally applied force. The resultant position of the mass

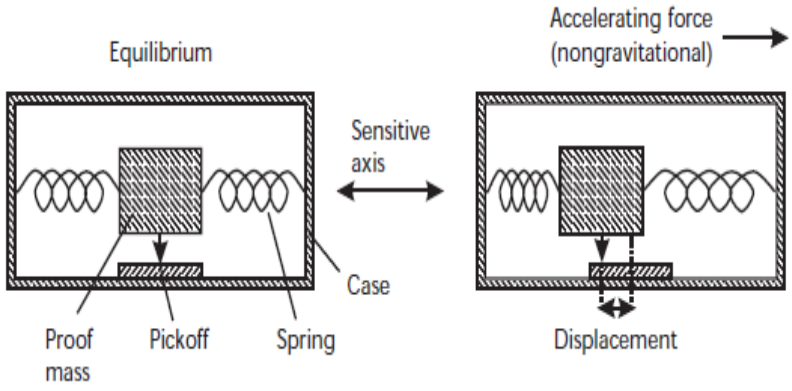

Figure 2.3: A conventional mechanical accelerometer.

with respect to the case is proportional to the acceleration applied to the case. By measuring this with a pick-off, an acceleration measurement is obtained. The exception to this is acceleration due to the gravitational force. Gravitation acts on the proof mass directly, not via the springs, and applies the same acceleration to all components of the accelerometer, so there is no relative motion of the mass with respect to the case.

Some of the most known mechanical accelerometers are: restrained pendulum (open loop), pendulous hinge elements (open loop), and two-axes force-feedback accelerometers (closed-loop).

The restrained pendulum accelerometer is mainly composed by a pendulum, a hinge element, a pick-off device, a torquer and a case.

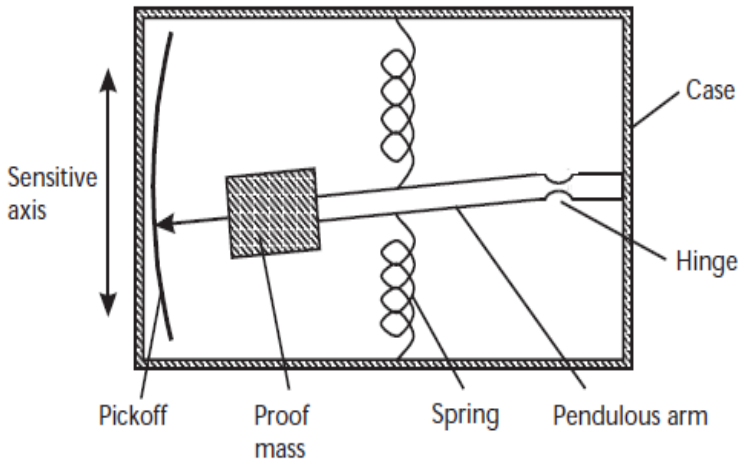

Figure 2.4: Pendulous-based accelerometer.

The deviation of the pendulum produced by an acceleration is sensed by the pick-off device, which in the most simple cases is directly measured from the displacement, but generally this kind of device operates with an electronic re-balance loop to feed the signal back in the pick-off to the torquer. The current in the torquer is proportional to the applied acceleration [1] [27].

The hinge element of a pendulous accelerometer is the component that enables the mass to move in a plane normal to the hinge axis. The two basic types of hinge elements are flexures and pivots, having several variations of each form.

In the flexure hinges, a low mechanical hysteresis material to minimize undesirable spring torque errors, is used. The main advantage of this type of flexure hinges is its very low static friction offering almost infinite resolution and low threshold. In the downside these devices have a very significant temperature dependent bias requiring calibration and compensation for must accurate applications.

The pivot hinges supports the pendulum between two spring synthetic jewel assemblies. This type provides a very small temperature dependent bias characteristics, but wearing the pivots in very discordant environment can be a serious problem [6].

The two-axes force-feedback accelerometer has many applications such as inertial navigation systems in ships. This sensor has a pendulum which freely swings about two orthogonal axes. It is restrained to its "null" position by electrical coils working in a permanent magnetic field. The principle of operation is identical the previous described sensors having a performance similar to the higher grade single axis devices [6].

2.3 Sensors based in optical technologies

2.3.1 Optical gyroscopes

The optical gyros use the properties of electromagnetic radiations, usually visible and infrared wavelengths, to sense the rotation. Therefore, it is possible to consider electromagnetic radiations as the inertial element of these sensors.

The principle behind this kind of gyros is the Sagnac effect [28], reported in 1913. When the light travels in opposite directions around an enclosed ring, differences come out in the optical length of the two paths when the ring is rotated around an axis orthogonal to the plane containing the ring.

The developments of these sensors are more recent than the mechanical gyros. The performance range of optical gyros is similar to that covered by mechanical sensors, but they offer several advantages over the mechanical gyros, such as [1]

- wide dynamic range
- instant start-up
- digital output
- independent of some enviromental conditions (accelerartion, vibration)
- high rate capability
- easy self-test
- system design flexibility

- extended running life

The principle of operation of optical gyros rely on the detection of an effective path length difference between two counter-propagating beams in a closed path, which arises with the presence of the turn rate applied around an axis perpendicular to the plane containing the optical paths. The transit time, which is the time the light beam employs to travel a complete round of the ring path, is identical for both beams when the ring is stationary [1].

When the ring is rotated with an angular velocity Ω, the transit of each beam change. Generally, the light travelling with the direction of rotation must travel further than when the interferometer is stationary [29]. The opposite will happen with the light beam travelling against the direction of rotation. The resultant beam at the output experiments a relative phase shift proportional to the undergoing rotation rate, due to the beams require different times to complete a trip around the rotating path.

Fiber Optic Gyros (FOG) and Ring Laser Gyros (RLG) [4] [30] provide performance degrees for applications oriented to higher precision as torpedos, air/land/sea navegation, geo-referencing mapping, surface and under surface surveying and navigation.

Ring Laser Gyroscopes

Ring Laser Gyroscopes (RLG) are based in the Sagnac effect, as explained in the previous section. Research had led to very low bias devices, with tyical path length in the order of 300 mm, but some investigation groups have developed devices of 50 mm.

The difference between the RLG and the FOG relies in the fact that in the RLGs the beams are addressed in a closed path employing mirrors instead of fibers. The principle of operation relies on a laser acting as an optical frequency oscilator using three or more mirrors to form a continous light path, such as a triangular shaped path when three mirrors are used [1]. When a light beam is generated, it travels around the closed path by reflecting in each mirror, forming the clockwise and the counter-clockwise beams, Fig. 2.5.

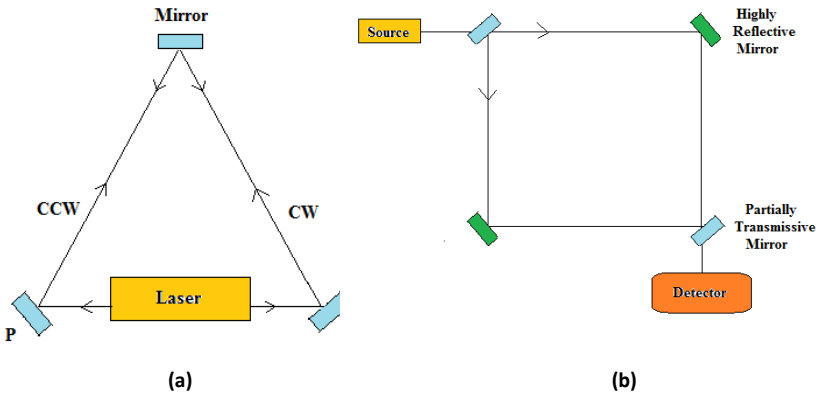

Figure 2.5: (a) Active RLG and, (b) Passive RLG.

RLG highlights by the method employed to overcome or reduce the lock-in effect, which occurs at low rotational rate, when both laser beams cease to oscillate at different frequencies causing the absence of ouput signal. The lock-in is eliminate by introducing a mechanical dither, a magneto-optic biasing or by the use of multiple optical frequencies [1].

The RLGs are well established today in the market of medium and high performance. This kind of gyroscope provides lot of advantages over mechanical gyros as high sensitivity and stability, quick start up, insensitivity to acceleration and inmunity to most enviromental effects. In the downside, as limitations, it can be pointed the restricted manufacturing of the exact ring cavity dimensions and the precision mirror, which also requires a very demanding clean room enviroment, which makes this option not suitable for low or economic performance applications. Other drawbacks are the size/weight, as well as the the high power requirements needed to supply the lasing media.

Fiber optic gyroscopes

Fiber optic gyros (FOG) consist in a long fiber optic coil, and use the light interference to measure the angular velocity by detecting the phase difference between the two beams passing the path in opposite directions, working as a Sagnac interferometer. In its simpler form, the light coming form a source is divided in two counter-propagating beams which are combined after the path length. An interference pattern is formed and the resultant intesity is detected by a photodetector. When the sensor is rotated, a path difference appears for the propagating beams, causing a change in the amplitude pattern, which is detected by the photodetector.

At present there are two classes of FOGs, the Interferometric FOG (IFOG) and the Resonant FOG (RFOG). The latter, the RFOG, has received less attention to date, and even it seems to offer better potential accuracy, is the less mature technology [31].

RFOG requires a narrowband light source and relies on an optical cavity which is formed by a optic fiber tuned, fostering a single frequency to propagate. If a rotation is applied, the frequency changes. The fiber resonator is formed by a few coils of fiber and a beam splitter; two input ports place the beams which are produced by the same coherent source, Fig 2.6.

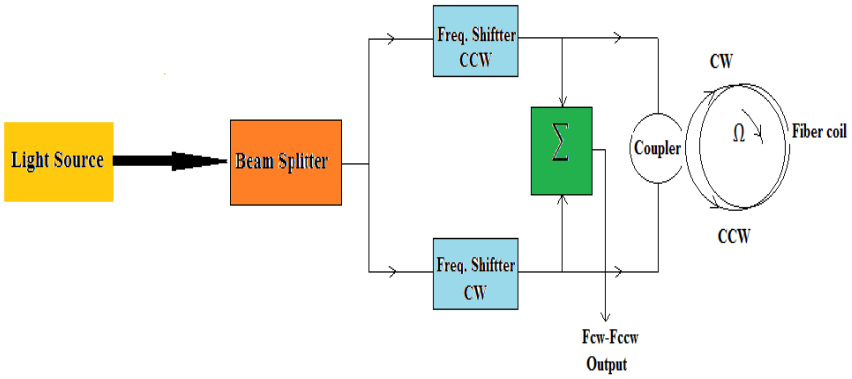

Figure 2.6: Resonant fiber optic gyroscope scheme [31].

In IFOGs devices, the Sagnac effect generates an optical phase difference between two counter-propagating waves in a rotating fiber coil, which is an indirect measurement of the rotation rate Ω. Longer coils increase the sensitivity, but at the same time they are more sensitive to temperature variation and vibration.

IFOGs can operate with two main configurations: open loop and closed loop. In the open loop configuration, the angular rate information is obtained directly through the output electrical signal.

Fig.2.7(a) shows an open loop IFOG scheme which is called "minimum configuration" meaning that this scheme guarantees the system reciprocity.

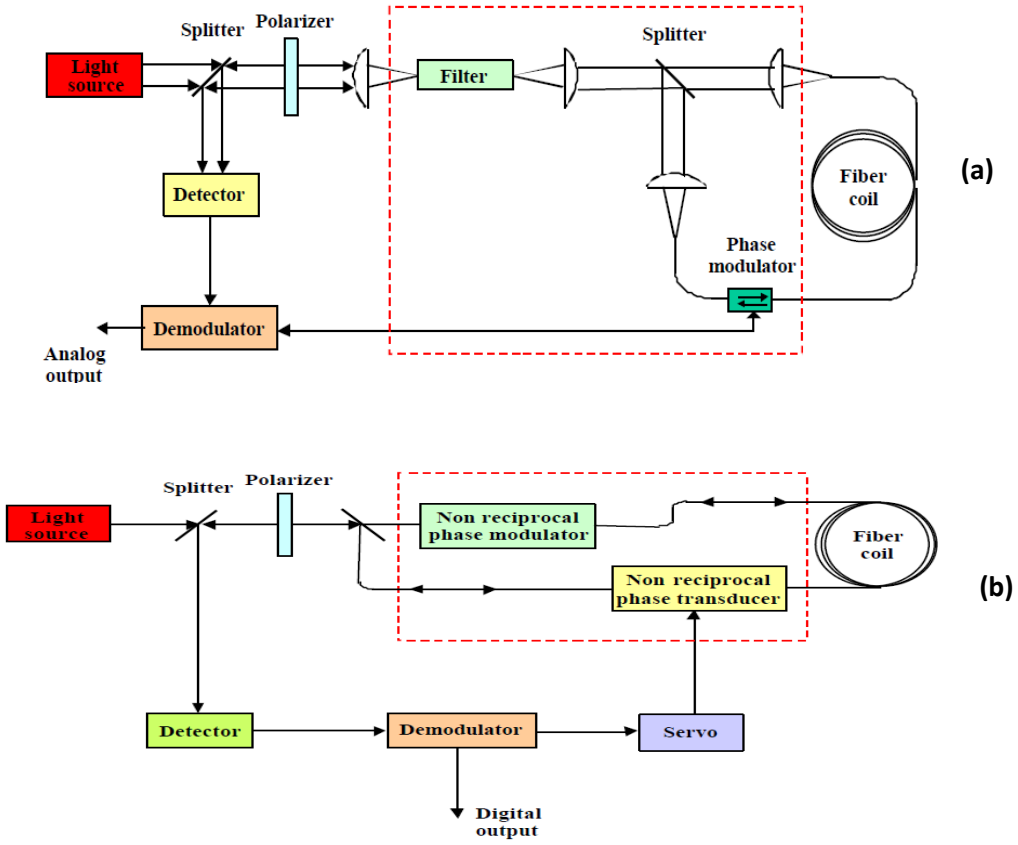

Figure 2.7: (a) Open loop, and (b) Closed loop interferometric optical gyroscope schemes [32].

The drawbacks of this configuration is the use of a very long fiber, the drift caused by the analog components and the influence of temperature.

To overcome the disadvantages of the open loop configuration, a closed loop can be used. This scheme is depicted in Fig. 2.7(b). The advantages of the closed loop versus the open loop is insensitivity to light intensity variations, which implies a very low drift.

FOGs are much less demanding in their fabrication techniques and much more flexible in their design and packaging than the RLGs.

2.3.2 Other optical technologies for gyros

Advances in photonics had led to newer gyro devices, as can be photonic cristal fiber (PCF) gyros, ring resonator gyros, integrated optical gyros, etc.

The advantageous use of PCF relies in the fact that these fibers have a pattern of holes in the structure that provides a hight quality in the light guiding with very low losses. These PCFs

gives very tight optical mode confinement making possible single mode propagation over many wavelengths, so tighter coils can be produced which translates in smaller packages. Also dispersion compensation can be embeeded in these fibers, reducing the spectral distortion on the performance of the sensor.

The ring resonator gyroscope has a ring formed by an optical waveguide with typical ring diameters of 50 mm. This type of sensor is known as micro-optic gyroscope (MOG), and when the problems associated to scattering and coupling can be overcome in these devices, the gyroscope on a "chip" can become a reality, along with all the advantages of optical sensors [33].

Developments of integrated optical gyroscope are considered highly desirable, as a "gyroscope on a chip" approach. The sensing element relies on an optical waveguide with the light travelling in opposite directions. These devices are built on a wafer and combine electromechanical processes and integrated optical fabrication. This type of sensing offers significant reduction in size in the order of 20 compared with conventional gyros, besides a power consumption reduction by a factor of 5. The fabrication of these devices are quite challenging nowaday, but many effort are addressed in this direction.

2.3.3 Optical accelerometers

Fiber optic accelerometer

The principle of operation of this kind of accelerometer is identical to the mechanical ones. The main difference lies in the pick-off and pendulum mechanisms which allow accelerations about two axes. These devices have excellent mechanical strenght and elastic characteristics and negligible thermal expansion over their normal operation temperature. The pendulum consists in a piece of optic fiber with a mass attached with a micro-lens at the bottom of the fiber and a solid-state laser coupled in the top.

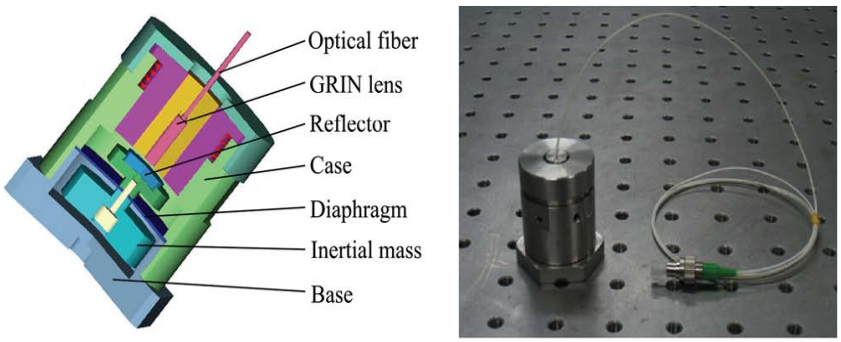

Figure 2.8: Fiber optic accelerometer.

When an acceleration is applied to the case containing this accelerometer, the bottom is deflected and the displacement is sensed and measured, the light emitted by the laser through the fiber is

focused on to two-dimensional photo-sensitive array, e.g. a charge coupled imaging device (CCID) which can provide x and y coordinates of the displacement. Currently, the accuracy is limited by the pixel density of the CCID [1] [34] [35].

Mach-Zehnder interferometric accelerometer

A Mach Zehnder interferometer can use one or two optical fibers attached to a mass [36]. When an acceleration is applied, the optical fiber experiments a small change in length which is proporcional to the acceleration, and this change can be detected by interferometric techniques. Using two fibers allows to form an arm an the use of nulling techniques enables greater sensitivities [1] [37].

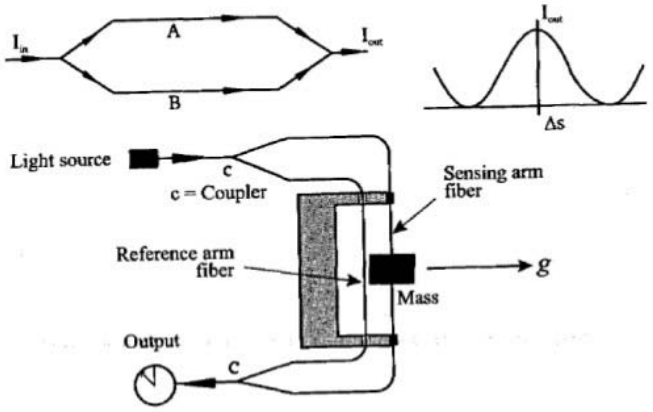

Figure 2.9: Mach Zehnder interferometric accelerometer.

Photo-elastic optic accelerometer

This tye of sensor is the target of lot of research nowaday. In this type of device the sensitive element is a birefringent material. The polarised light is launched into the birefringent material trough a fiber, and when an acceleration is applied to the photo-elastic material the light changes proportionally to the acceleration and measured by a detector, as shown in Figure 2.10.

Bragg grating fiber accelerometer

Several research centers have developed accelerometers based in Bragg gratings [38]. The principal wavelenght of the Bragg grating is set by its characteristic but ib can be changed with the changes in temperature, strain and pressure on the grating. Therefore, when an acceleration is applied, the grating wavelenght changes proportionally to the acceleration and can be detected using a fiber interferometric. Still the performance of such device is not clearly established, but initial research has shown good sensitivities.

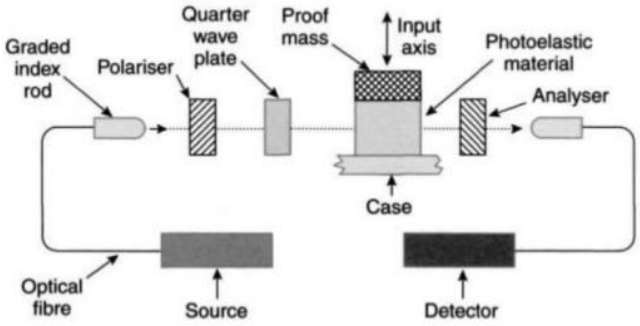

Figure 2.10: Photo-elastic fiber optic accelerometer [1].

2.4 Micro Electro-Mechanical System Sensors

2.4.1 Introduction

New applications demanding low-cost sensors have triggered the development of micro-electro-mechanical system sensors (MEMS). MEMS sensor is one of the most exciting field in the last 25 years. Current inertial sensor development is focused on micro electro-mechanical system (MEMS) technology. This enables quartz and silicon sensors to be mass produced at low cost using etching techniques with several sensors on a single silicon wafer. MEMS sensors are small, light and exhibit much greater shock tolerance than conventional mechanical designs. However, they currently offer relatively poor performance. These devices have become crucial in applications where cost, size and lower power consumption are keys. The use of silicon and quartz as base materials yield to achieve these parameters. The properties of the resulting sensors are [1]

- small size;
- low weight;
- rugged construction;
- low power consumption;
- short start-up time;
- inexpensive to produce in high volume;
- high reliability;
- low maintenance;
- operational in hostile environments.

These features provide to the engineers a design flexibility beyond any technology preceeding these developments. Therefore, many applications, both commercial and militar, have been proliferated in the last years. The drawbacks lie on critical performance parameters as the angle random walk, which is very important in stabilization and positioning systems; they also have bigger bias instability, which degradates the navegation and stabilization/positioning solutions.

Despite these limitations, MEMS sensors approaching sensitivities of $1°/h$ are expected to become reality in the next few years. Consequently, the inertial sensor technology researches have been focused almost exclusively in the development and improvement of MEMS devices.

Nowadays, MEMS are tipically used in consumer and industrial applications as digital cameras, smartphones, videogame controllers, automotive purposes, AHRS miniaturization, inteligent ammunition, robotics, etc [16].

2.4.2 MEMS gyros technology

MEMS gyros are non-rotatory devices and use the Coriolis effect on a vibrating mass(es) to detect angular rotation. Thus, these sensors detect the force acting over a mass which is subject to a lineal vibratory motion in a frame of reference, and is rotating about an axis perpendicular to axis of the linear motion. The resultant force, the Coriolis force, acts in a direction which is perpendicular to both axes, the vibratory and the axis around the rotation is applied [39].

The MEMS gyros available can be classified as follows: vibrating beams, tuning fork, vibrating shells and vibrating plates [32]. The operating principle is the same for all of them. The tuning fork configuration, is shown in Fig. 2.11. In this case, two masses oscilate and move in opposite directions. When an angular velocity is applied, the Coriolis force to act each mass in opposite direction resulting in a capacitance change, which is proportional to the angular velocity and it is converted in an output voltage for analog devices or LSBs for digital ones. When a linear velocity is applied, both masses move in the same direction, and no capacitance difference is detected, thus, MEMS gyros are not sensitive to linear acceleration [40].

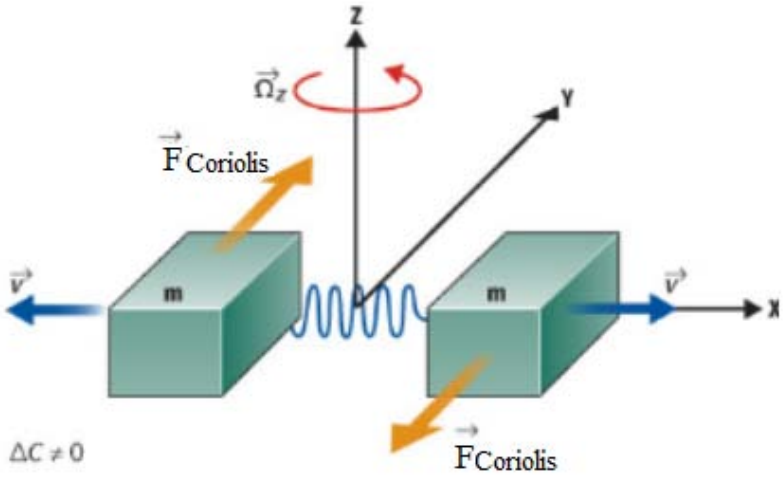

Figure 2.11: MEMS gyroscope with tuning fork configuration [40].

Vibrating structures have been sucessfully used to detect turn rates. These structures have the

advantage to keep the drive and sense vibrational energy in a single plane, but suffer a relatively low vibrating mass and therefore, exhibit a low-scale factor.

A new approach to MEMS is the micro-opto electromechanical systems (MOEMS). This technology offers a true solid-state sensor with an optical readout, overcoming the lack of the MEMS performance for measuring small displacements [1].

2.4.3 MEMS accelerometer technology

As in the case of gyros, the use of silicon to manufacture accelerometers is well established. MEMS accelerometers can be divided in two classes taking into account the way the acceleration is sensed:

- the displacement of a mass sustained by a hinge or a flexure in the presence of an acceleration.
- the change of frequency of a vibrating element caused by the change in tension as a result of an acceleration.

Several types of MEMS acceleremoters are available in the market, as the pendulous mass, resonant, tunneling and electrostatically levitate MEMS acceleremoters.

Pendulous mass MEMS accelerometer has the advantage its versatility of packaging, allowing planar mounting of the device. This type of sensor has found many applications in the militar industry, such as guide-munitions applications [41]. Figure 2.12 shows an in-plane pendulous MEMS acceleremoter. Acceleration is measured by detecting the change in capacitance across the sensing element, being more sensitive in the horizontal plane than in the orthogonal direction [1].

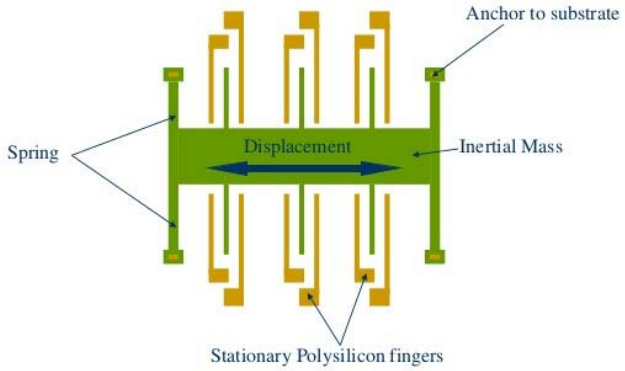

Figure 2.12: MEMS pendulous accelerometer.

Resonant MEMS accelerometers can sense acceleration acting in the planar and the perpendicular axes of the accelerometer, which can measure acceleration as the result of the change of the resonant frequency of beam oscillators under inertial loading of a mass instead of a displacement's measurement. Silicon and quartz have been used to manufacture these sensors [42].

Tunneling MEMS accelerometers offer enhancements over the previous analized devices, offering better resolution, higher bandwidth and small packaging. They are based on bulk silicon

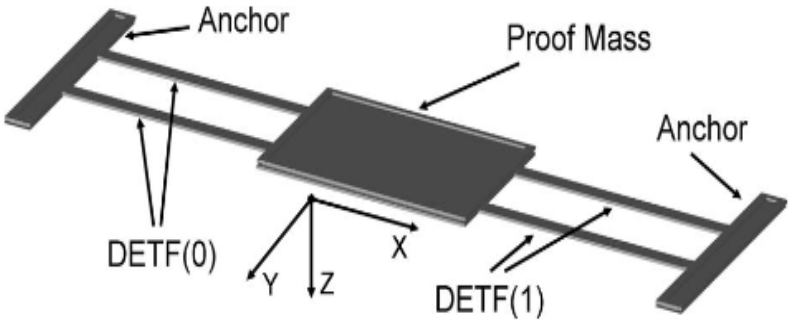

Figure 2.13: MEMS resonant accelerometer.

micromachining, normally incorporating boron etch-stop wafer processes. Some of the main physical components in a tunneling accelerometer include a proof-mass, a tunneling tip and a counter electrode [43].

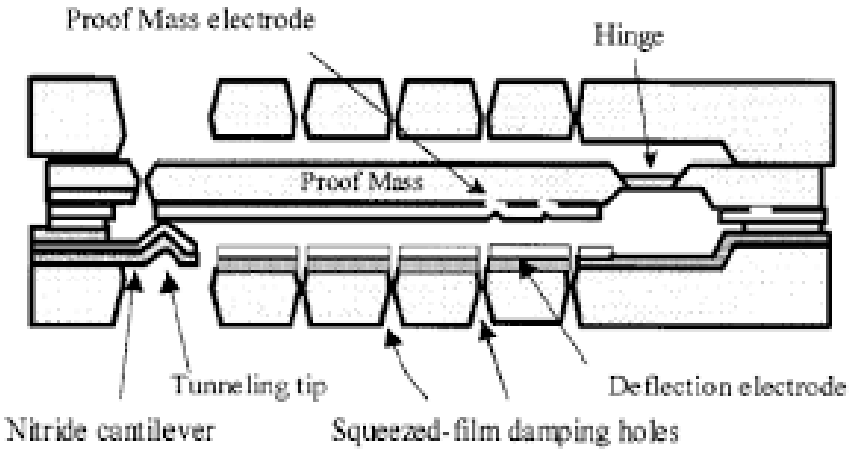

Figure 2.14: Tunneling MEMS accelerometer.

2.5 Inertial sensor error and noise characteristics

2.5.1 Introduction

This section will show a review of the most common errors and noises in gyroscopes and accelerometers and their effects on the integrated output signal. The predominant error and noise sources are: constant bias error, bias instability, angle random walk (gyros) and velocity random walk (accelerometer), quantization, rate angle walk, rate ramp and sinusoidal component.

2.5.2 Constant bias error

The sensor bias is the average output of the device over a specified time measured in specific operation conditions which have no correlation with the sensor rotation (gyros) or input acceleration (accelerometer). The bias is typically expressed in degree per hour ($^\circ/h$) or radian per second (rad/s) for gyros, and in meter per second squared (m/s^2 or g). The bias generally consists in two parts: one deterministic part called bias offset and a random part. The bias offset, which is the offset in the measurement provided by the inertial sensor can be determined by calibration [12] [44]. The random part is a stochastic process and refers to the rate at which the error in an inertial sensor accumulates with time.

2.5.3 Bias instability

Additionally, there are two characteristics used to described the sensor bias: the bias asymmetry, which is the difference between the bias for positive and negative inputs; and the bias instability, which is the random variation in the bias computed over a finite sample of time. This effect affects both gyros and acceleremoters.

Usually, it is interesting to know how this error affects the orientation obtained through integration the rate gyro/accelerometer signal.

The rate power spectral density (PSD) associated with the bias instability, also known as $1/f$ noise is

$$S_\Omega(f) = \begin{Bmatrix} \left(\frac{B^2}{2\pi}\right)\frac{1}{f} & f \leq f_0 \\ 0 & f > f_0 \end{Bmatrix}, \tag{2.1}$$

where B is the bias instability coefficient and f_0 is the $3dB$ cutoff frequency.

2.5.4 Angle random walk/velocity random walk

An angular/velocity rate sensor measures the rotation/displacement rate over its sensitive axis. The sensor output signal is perturbed by a type of thermo-mechanical noise fluctuating in a bigger rate than the sample rate of the sensor, called angle/velocity random walk (ARW/VRW). The ARW/VRW is a noise specification given in units of $^\circ/\sqrt{h}$ for gyros, and $m/s/\sqrt{h}$ for accelerometers, which is directly applicable to the computation of the angle/velocity. As consequence, the samples obtained are disturbed by a white noise, which is a sequence of uncorrelated random variables and mean zero.

ARW/VRW describes the average deviation or the error that will occur when the signal is integrated. This error increases with the integration time, and provides a fundamental limitation to any angle/velocity measurement based only on integration of a rate [45].

For instance, an $ARW = 0.1^\circ/\sqrt{h}$ means that after 1 hour the angle deviation is 0.1°; after 2 hours working, $ARW = 0.1^\circ/\sqrt{h} \cdot \sqrt{2} \approx 0.14^\circ$.

As mentioned, this term of noise is characterized by a white noise spectra on the gyro rate output, which is a random noise with a constant power spectral density (PSD) independent of frequency.

The associated PSD is given by [13]

$$S_\Omega(f) = Q^2, \tag{2.2}$$

where Q is the angle randow walk coefficient expressed in $^\circ/h/\sqrt{Hz}$, describing the output noise as a function of the sensor bandwidth.

Generally, the manufacturers quote noise specifications in different ways: an ARW/VRW, a PSD or FFT noise density and with one or three σ variation in the output sensor. Estimating the ARW/VRW given these parameters, is well stablished in the IEEE Std. 952-1997 C.1.1 In the case of ARW

$$ARW(^\circ/\sqrt{h}) = \frac{1}{60}\sqrt{PSD[(^\circ/h)^2/Hz]}, \tag{2.3}$$

$$ARW(^\circ/\sqrt{h}) = \frac{1}{60}FFT(^\circ/h/\sqrt{Hz})), \tag{2.4}$$

$$ARW(^\circ/\sqrt{h}) = \frac{1}{60}\sigma(^{\circ/h})\frac{1}{\sqrt{BW}(Hz)}, \tag{2.5}$$

where σ is the standard deviation of the signal and BW is the effective bandwidth of the sensor in Hz.

2.5.5 Quantization noise

This noise is introduced into an analogic signal as the result of encoding it into a digital signal. This is caused by the differences between the real amplitudes of the points sampled and the analog-digital converter resolution .

The angle PSD is given as (IEEE 952 1997)

$$S_\theta(f) = TQ^2\left\{\frac{\sin^2(\pi fT)}{(\pi fT)^2}\right\} \approx TQ^2, \tag{2.6}$$

for $f << \frac{1}{2T}$; Q is the quatization noise coefficient and T is the sample interval.

The theoretical limit for Q is $S/\sqrt{12}$, where S is the sensor-scaling coefficient for tests with uniform and fixed sample times [46] [44]. The rate PSD is related to the angle PSD through the expression

$$S_\Omega(2\pi f) = (2\pi f)^2 S_\theta(2\pi f). \tag{2.7}$$

Therefore,

$$S_\Omega(f) = \frac{4Q^2}{T}\sin^2(\pi fT) \approx (2\pi f)^2 TQ^2, \tag{2.8}$$

for $f < \frac{1}{2T}$.

2.5.6 Rate random walk

This is an error of unknown origin, with a rate PSD associated (IEEE 952 1997)

$$S_\Omega(f) = (\frac{K}{2\pi})^2\frac{1}{f^2}, \tag{2.9}$$

where K is the rate random walk coefficient.

2.5.7 Rate ramp

For long but finite time spans, this error is more a deterministic error than a random noise. The rate ramp is defined as (IEEE 952 1997)

$$\Omega = Rt, \tag{2.10}$$

where R is the rate ramp coefficient.

The rate PSD associated with this noise is

$$S_\Omega(f) = \frac{R^2}{(2\pi f)^3}. \tag{2.11}$$

2.5.8 Sinusoidal noise

This noise is characterized by s number of different frequencies. A representation of the PSD, which contains a single frequency is given by (IEEE 951 1997)

$$S_\Omega(f) = \frac{1}{2}\Omega_0^2[\delta(f - f_0) + \delta(f + f_0)], \tag{2.12}$$

where Ω_0 is the amplitude, f_0 is the frequency and $\delta(x)$ is the Dirac delta function.

Several frequencies sinusoidal errors can be represented by a sum of terms with equation 2.12 with their frequency and amplitude, respectively.

2.6 Inertial sensor trends

As shown in this Chapter, there are many sensor types and technologies, which are used to detect or measure an angular motion, in case of gyros, and acceleration in the case of accelerometer. A great effort has been put to develop the so called "sensor on a chip". New technologies used in the industry, as robotics, hold this effort. Several sensors show an undesired sensitivity under certain environments, thus, the goal of researchers involved in this field, has been to reduce these sensitivities. Generally, a significant amount of precision engineering and high technology is needed to produce a functional device. At short-mid term, despite the advances in optical devices, applications needing very high performance ($10^{-4} - 10^{-5^\circ}/h$) are still addresed to mechanical sensors. To mid-range performance requiring a high stabilitaty factor, optical sensors are a good choice.

For MEMS devices a continous improvements are required, it means, special care in the material uniformity, robust vacuum packaging and tuning in frequency to compensate the sensor drift. Also, a low noise and low drift electronic circuitry are needed.

In log-term, MEMS sensors will improve and will find a niche in high performance applications. MEMS and integrated optic devices also will dominate in the low and medium performance range, while optical will dominate when a high factor of stability is needed. For this, optical MEMS (MOEMS) sensors are under development since several years ago, but their design is very difficult due to their small dimensions [47]. Also, integrated optic versions of inertial sensors with the target of a very small size and low cost are currently investigated [48].

Chapter 3

Allan Variance method and denoising

3.1 Introduction

Within the noise analysis methods, the PSD and Allan variance methods have been adopted as preferred means of analysis in the inertial systems community for having more general application on stochastic models (IEEE Std 952-1997).

The frequency-domain approach for modeling noise by using PSD to estimate the transfer functions is straightforward but difficult to understand for nonsystem analysts. In the other hand, Allan variance is simple to compute and relatively simple to interpret and understand as well as accurate enough in modeling noises.

Since a low-cost INS (MEMS grade) presents error sources with short-term (high-frequency) and long-term (low-frequency) components, we introduce wavelet denosing and averaging filter. Wavelet is specially powerful removing high frequency components. Wavelet de-noising has been used in similar works, because of its great effectiveness removing high-frequency noises, as it is shown in [49][50][51].

This Chapter is focused in the Allan variance method, and in the Wavelet transform which will be described in the next sections.

3.2 Allan variance method overview

The Allan Variance (AVAR) method was proposed by David Allan in 1966 as a simply variance analysis method, and it was widely adopted for the characterization of phase and frequency instability of precision oscillators [11]. In 1998, the IEEE standard introduced the AVAR as a noise identification method for linear accelerometer analysis (IEEE Std1293-1998).

The AVAR method was first applied to MEMS device noise identification by Hou and El-Sheimy in 2003 [12].

AVAR is a time domain analysis technique originally designed for characterizing noise and stability in clock systems, and it is an accepted IEEE standard for gyro specifications [11]. The technique can be applied to any signal to determine the character of the underlying noise processes, and can be applied to analyse the error characteristics of any precision measurement instruments [46].

It is a method of representing root mean square (RMS) random drift error as a function of average time, and can be used to determine the character of the underlying random processes

that give rise to the data noise. By performing certain operations on the entire length of data, it is employed to characterize various types of noise terms in the inertial sensor data [52]. Its value, however, depends upon the degree of understanding of the physics of the instrument. The uncertainty in the data is assumed to be generated by noise sources of specific character. The key attribute of the method is that it allows for a finer, easier characterization and identification of error sources and their contribution to the overall noise statistics.

In the next section, the relationship between the AVAR and the noise PSD is established. Using this relationship, the behavior of the characteristic curve for a number of prominent noise terms can be determined.

3.3 Allan variance principles

AVAR is based in the method of cluster analysis. The data flux is divided in clusters of a specific length. Given N consecutive data points, each one having a sample time t_0. Forming a group of n consecutive data points (with $n < N/2$), each group is a cluster as shown in Fig. 3.1. The number of clusters is $K = N/n$.

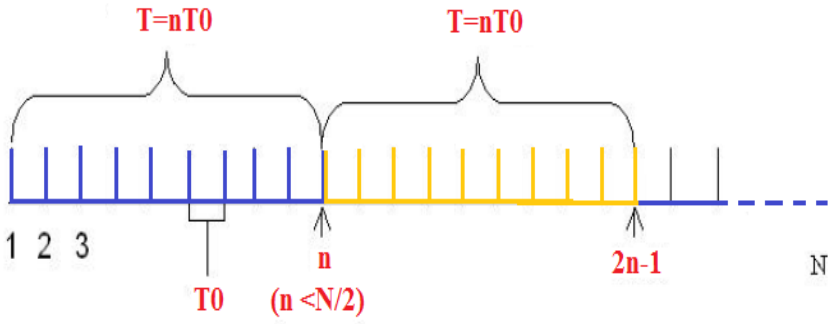

Figure 3.1: Schematic of the data structure used in the derivation of Allan variance [52].

A modified version of AVAR analysis is the overlapped AVAR, which is depicted in Figure 3.2. In this version, a cluster overlaps the previous one, achieving an exhaustive use of the dataset. The analysis here is the same as in the case of the standard AVAR. Therefore, the analysis review that will be carried out is valid for both variants.

Associated with each cluster, there is a period T, which is equal to nt_0. If the instantaneous output rate of inertial sensor is $\Omega(t)$, the cluster average is computed as [13]

$$\overline{\Omega}_k(T) = \frac{1}{T}\int_{t_k}^{t_k+T} \Omega(t)\, dt \tag{3.1}$$

where $\overline{\Omega}_k(T)$ represents the average output rate of the cluster which starts at the k^{th} data point and contains n data points.

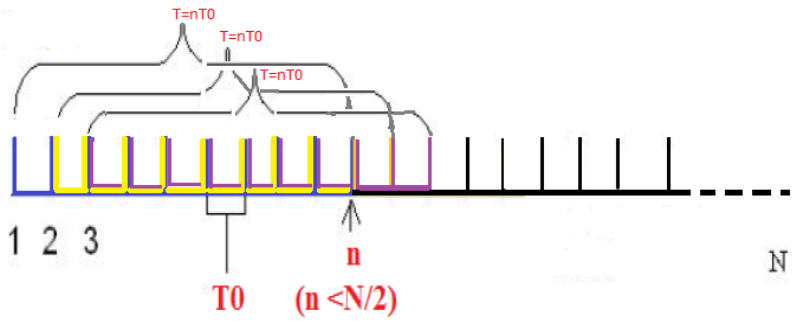

Figure 3.2: Schematic of the data structure used in the derivation of overlapped Allan variance.

The subsequent cluster average is given by

$$\overline{\Omega}_{next}(T) = \frac{1}{T}\int_{t_k+T}^{t_k+2T} \Omega(t)\, dt. \tag{3.2}$$

The AVAR of length T computed from two adjacents clusters is (IEEE Std952-1997)

$$\sigma^2(T) = \frac{1}{2}\langle[\overline{\Omega}_{next}(T) - \overline{\Omega}_k(T)]^2\rangle \equiv \frac{1}{2(K-1)}\sum_{k=1}^{K-1}[\overline{\Omega}_{next}(T) - \overline{\Omega}_k(T)]^2, \tag{3.3}$$

where $\langle\rangle$ denotes ensemble average.

Selecting different cluster lengths or correlation time for each calculation of AVAR, it is possible to obtain the AVAR as a function of the correlation time. This method, in a log-log plot, can discriminate the different contributions of the errors by examining the varying slope of the plot, which is normally plotted as the square root of AVAR versus T. If the the proper values of the correlation time is chosen, information about the angle random walk, quantization noise, bias instability, etc., can be found. The diverse random process causes slopes, each one with a proper gradient, and usually appear in different position in the curve, allowing to be identified in a straightforward way.

It is feasible to establish a relation between AVAR and the two sided rate noise PSD. The PSD is a common way to represent the spectral decompositition of a time series, turning it into a powerful tool to analyze data from stochastic models. The relation between the PSD $S(\omega)$ and the covariance $K(\tau)$, is expressed as [13]

$$S(\omega) = \int_{-\infty}^{\infty} e^{-j\omega\tau}K(\tau), d\tau. \tag{3.4}$$

The AVAR can be defined in terms of output angle or velocity as (IEEE Std 952-1997) [44]

$$\theta(t) = \int^{t} \Omega(t), dt, \tag{3.5}$$

where the lower limit of the integral is not especified as only angle or velocity differences are employed in the definitions.

The angle or velocity measures are done in discrete times given by $t = kt_0$, $k = 1, 2, 3..., N$. The notation is simplified as $\theta_k = \theta(kt_0)$. The cluster averages can be rewritten as

$$\overline{\Omega}_k(T) = \frac{\theta_{k+n} - \theta_k}{T}, \tag{3.6}$$

and

$$\overline{\Omega}_{next}(T) = \frac{\theta_{k+2n} - \theta_{k+n}}{T}. \tag{3.7}$$

Therefore the AVAR can be found as

$$\sigma^2(T) = \frac{1}{2T^2(K-1)} \sum_{k=1}^{K-1} (\theta_{k+2n} - 2\theta_{k+n} + \theta_k)^2. \tag{3.8}$$

The equivalent relation between the AVAR and the PSD is given by the expression [46] [13]

$$\sigma^2(T) = 4 \int_0^\infty df \cdot S_\Omega(f) \frac{\sin^4(\pi f T)}{(\pi f T)^2}, \tag{3.9}$$

where $S_\Omega(f)$ is the PSD of the $\Omega(T)$ process, which is assumed to be stationary in time.

Equation 3.9 is the focal point of the Allan variance method. This equation will be used to calculate the Allan variance from the rate noise PSD. The PSD of any physically meaningful random process can be substituted in the integral, and an expression for the Allan variance $\sigma^2(T)$ as a function of cluster length is identified. Conversely, since $\sigma^2(T)$ is a measurable quantity, a log-log plot of $\sigma(T)$ versus T provides a direct indication of the type of random process existing in the inertial sensor data. The corresponding Allan variance of a stochastic process may be uniquely derived from its PSD [44].

As explained in this section, AVAR is a very attractive method to sort the error components in the gyro output by their own slopes in the log-log plot.

3.3.1 Estimation accuracy of the Allan Variance

A finite number of clusters can be generated from any finite set of data. Allan variance of any noise term is estimated using the total number of clusters of a given length that can be created. Estimation accuracy of the Allan variance for a given τ, on the other hand, depends on the number of independent clusters within the data set (IEEE 952 1997).

The accuracy in the estimation of $\sqrt{AVAR}$ (RAVAR) increases with the number of clusters. Generally, the σ percentage of error of the computation for K clusters, while computing $\sigma(\tau)$ is [46]

$$\sigma(\%error) = \frac{100}{\sqrt{2(K-1)}}. \tag{3.10}$$

The number of clusters K is given by N/n where N is the length of the data set, and n is the number of points contained in a cluster. The estimation errors in the regions of short (long) τ are small (large) as the number of independent clusters in these regions is large (small). This equation can be used to design a test to observe a particular noise of certain characteristics to within a given accuracy, as explained in (IEEE 952 1997).

3.4 Allan variance analysis of the inertial sensor's noise sources

3.4.1 AVAR analysis of Bias Instability

Substituting the PSD associated with the bias instability, equation 2.1, in the AVAR expression 3.9 and performing the integration yields [46] [13]

$$\sigma^2(T) = \frac{2B^2}{\pi}\left\{\ln 2 - \frac{\sin^3 x}{2x^2}(\sin x + 4x\cos x) + C_i(2x) - C_i(4x)\right\}, \tag{3.11}$$

where $x = \pi f_0 T$ and C_i is the cosine-integral function; this expression can be simplified for $T >> 1/f_0$ as

$$\sigma(T) \to \sqrt{\frac{2\ln 2}{\pi}} B = 0.664B. \tag{3.12}$$

The bias instability value can be read off the RAVAR plot at the region where the slope is zero, as shown in Fig 3.3.

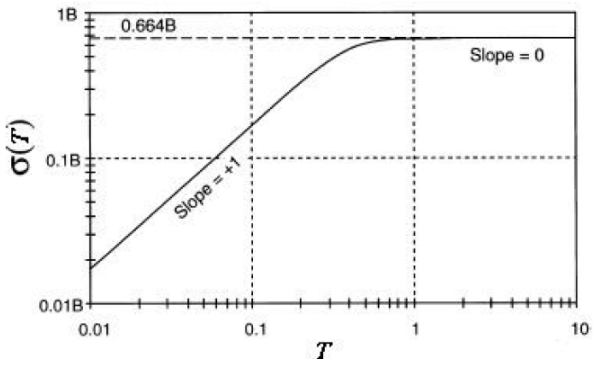

Figure 3.3: $\sigma(T)$ versus T plot for bias instability (for $f0 = 1$) (IEEE 952 1997).

3.4.2 AVAR analysis of ARW/VRW noise

Substituting the ARW/VRW PSD (2.2) in the AVAR expression of (3.9)

$$\sigma^2(T) = \frac{Q^2}{T}. \tag{3.13}$$

In the log-log plot of $\sigma(T)$ versus T, ARW has a slope of $-1/2$, as shown in Fig 3.4.

3.4.3 AVAR analysis of Quantization noise

Substituting equation 2.8 in the equivalent relation between the AVAR and the PSD (3.9) and performing the integration

$$\sigma^2(T) = \frac{3Q^2}{T^2}, \tag{3.14}$$

$$\sigma(T) = Q\frac{\sqrt{3}}{T}. \tag{3.15}$$

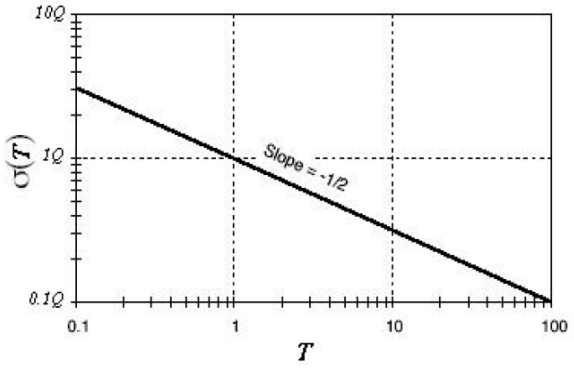

Figure 3.4: $\sigma(T)$ versus T plot for ARW/VRW noise (IEEE 952 1997).

Therefore, the quantization noise is represented by a slope of -1 in the log-log plot. The noise magnitude can be read in the slope line at $T = \sqrt{3}$.

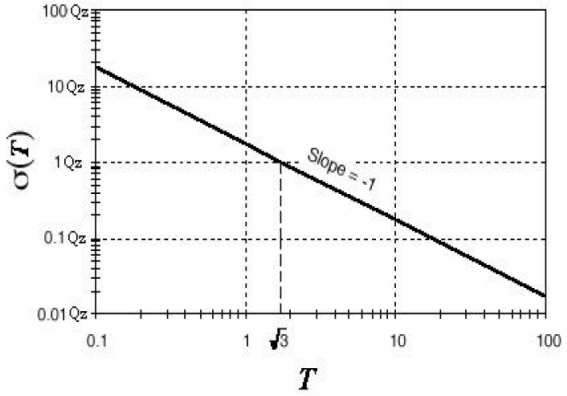

Figure 3.5: $\sigma(T)$ versus T plot for quantization noise (IEEE 952 1997).

3.4.4 AVAR analysis of Rate Random Walk noise

Substituting the expression of the rate random walk PSD (2.9) in the equation 3.9, and performing the integration

$$\sigma^2(T) = \frac{K^2 T}{3}, \tag{3.16}$$

thus

$$\sigma(T) = K\frac{T}{3}. \tag{3.17}$$

Therefore, this noise is represented by a slope of $\frac{1}{2}$ on a log-log plot of $\sigma(T)$ versus T. The magnitude of this noise can be read in this slope line at $T = 3$. The unit of K is usually given in $^\circ/h^2/\sqrt{Hz}$.

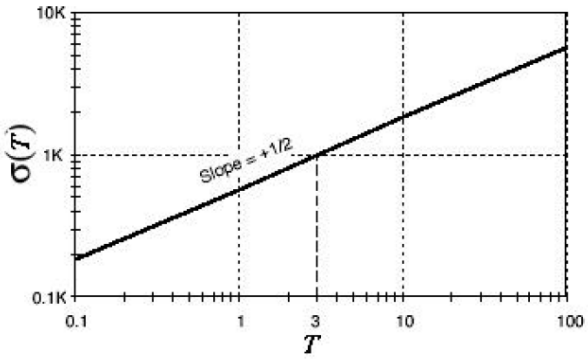

Figure 3.6: $\sigma(T)$ versus T plot for rate random walk noise (IEEE 952 1997).

3.4.5 AVAR analysis of Rate Ramp noise

Operating on the AVAR cluster containing an input given by 2.10, it is obtained

$$\sigma^2(T) = \frac{R^2T^2}{2}, \tag{3.18}$$

thus,

$$\sigma(T) = R\frac{T}{\sqrt{2}}. \tag{3.19}$$

Therefore, the rate ramp noise has a slope of 1 in the log-log plot. The amplitude R can be obtained from the slope line at $T = \sqrt{2}$, as can be viewed in Fig. 3.7

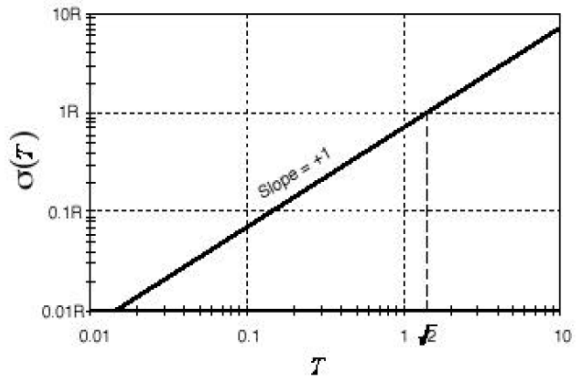

Figure 3.7: $\sigma(T)$ versus T plot for rate ramp noise (IEEE 952 1997).

3.4.6 AVAR analysis of Sinusoidal noise

Substituting 2.12 in the equivalent relation between the AVAR and the PSD (3.9), and performing the integration [46]

$$\sigma^2(T) = \Omega_0^2\left[\frac{\sin^2(\pi f_0 T)}{\pi f_0 T}\right]^2. \tag{3.20}$$

The AVAR of a sinusoid, when it is plotted in the log-log curve, indicates a sinusoidal behaviour with attenuate consecutive peaks at the slope of -1. The observation of this noise is difficult due to the fact that the peaks fall off rapidly and can be masked by higher order peaks of other frequencies [44].

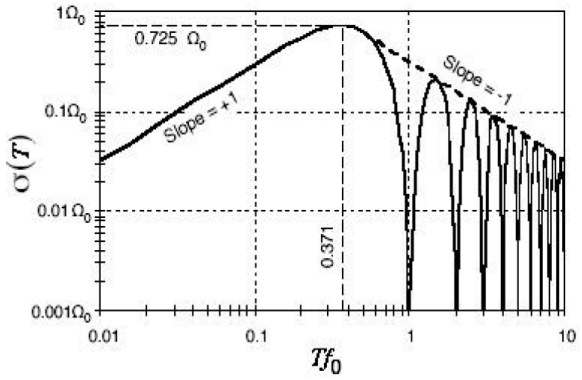

Figure 3.8: $\sigma(T)$ versus T plot for sinusoidal noise (IEEE 952 1997).

3.4.7 Combined effects of the noises

Generally, a number of error components are present in the data, depending of the device and on the enviroment in which the data is measured. If the noise sources are statistically independent , the computed AVAR is the sum of the square of each error as

$$\sigma^2_{total} = \sigma^2_{quant.} + \sigma^2_{ARW} + \sigma^2_{biasInst} + \sigma^2_{sin} + \sigma^2_{RRW} + .. \tag{3.21}$$

A typical AVAR plot looks like Fig.3.9, where the noise terms appear in different regions of T, which allow and easy identification of the random process existing in the data. A certain amount of error can be found in the curve due to the uncertainty of the AVAR measures [46] [44].

The error percentage in the estimation of $\sigma(T)$, with clusters containing M data points from N points data set, is given by [44]

$$\sigma = \frac{1}{\sqrt{2(\frac{N}{M} - 1)}} \tag{3.22}$$

3.5 Discrete wavelet transform for denoising

Wavelet analysis is a powerful method for decomposing and representing signals which has been used in a wide range of fields. Similar to the Fourier transform, wavelet can be used to analyze a time domain signal and transform it in frequencies components, based on analyzing a signal through signal windowing but with variable window size. Discrete wavelet transform (DWT) are used for discrete time signals [53].

Wavelets have been found to be a powerful tool for removing noise from a variety of signals (denoising). To use this method, it is not necessary to know the nature of the signal, and allows discontinuities and spatial variation of the signal.

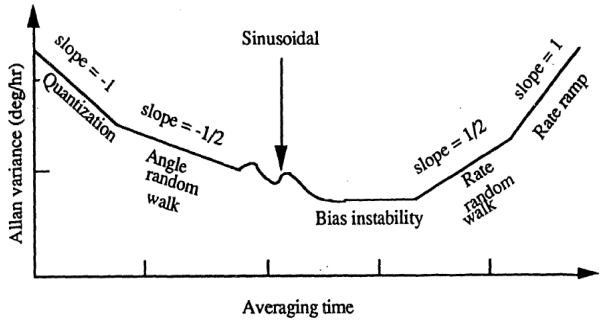

Figure 3.9: Plot of AVAR versus T [46].

A wavelet is a wave-like oscillation with an amplitude that starts out at zero, increases, and then decreases back to zero. Unlike the sines used in Fourier transform for decomposition of a signal, wavelets are generally much more concentrated in time [14] [15].

Given a mother wavelet $\psi(t)$ the continuous wavelet transform (CWT) of a function $x(t)$ is given by

$$X(a,b) = \frac{1}{\sqrt{a}} \int_{-\infty}^{\infty} \psi\left(\frac{t-b}{a}\right) x(t)dt, \tag{3.23}$$

where a is the dilation parameter which corresponds to frequency information, and b is the translation parameter which it is related to the location of the wavelet function as it is shifted through the signal, so it corresponds to the time information in the transform [14]. This expression is like a convolution between the signal and a wavelet basis function.

In the case of DWT, instead of working with a and b, the values of $X(a,b)$ are calculated over a discrete grid:

$$a = \alpha^n, b = m \cdot \alpha^n, \tag{3.24}$$

where n and m are integer numbers representing the discrete dilation and translation indices. It has been found that the most efficient way of determining a and b is the dyadic one, where $\alpha = 2$.

The basis function in equation (3.23) would be

$$\psi_{m,n}(t) = \frac{1}{\sqrt{2^n}} \psi\left(\frac{t}{2^n} - m\right), \tag{3.25}$$

The low frequency component of a signal is called the "approximation part" while the high frequency component is called the "detail part". The high frequency component usually constitutes the signal noise [44].

The methodology is to split the signal down into many-lower resolution components by repeating the DWT decomposition to obtain finer resolution frequency components. This procedure can be done repeatedly until the individual details consist on a sigle frame. Practically, an appropriate Level of Decomposition (LOD) is chosen based on the nature of the signal or on a specific criterion [15].

In this Thesis, the Wavelet toolbox of Matlab is used to perform the signal denoising, as it will be explained in the next Chapter.

Chapter 4

Test and Results

4.1 Introduction

This Chapter is devoted to the practical implementation of the overlapped AVAR method to characterize the different types and magnitudes of error terms existing in the IMU 3DM-GX3-25, which is composed by three gyroscopes and three accelerometers, together with other components. Once the AVAR is performed, a process of denoising, using the Wavelets Transform and Median Filter, is carried out.

To collect and to analyze the data for characterizing the noises, an experimental setup was assembled to gather static sensors readings. Three datasets with different duration, 9.5, 1, and 3.5 hours, were collected.

The AVAR method was coded in Matlab, and the Allan deviation plots were constructed for gyros and accelerometers for the different datasets. From the inspection and processing of the obtained characteristic curves, the magnitude and the type of the errors affecting our sensor, were determined and the quality of the sensor evaluated. After that, a process of denoising by using the Wavelets Transform and Median Filter were performed taking advantages of the Wavelet Toolbox of Matlab.

The next sections show the performed tests and the analysis of the obtained results.

4.2 Data acquisition and experimental setup

For the data acquisition, an experimental setup was held in a customized desk at room temperature for several days. The experimental setup involved: an IMU model 3DM-GX3 -25, a laptop model Dell XPS M1330 with operating systems Ubuntu 14.04, and a C++ driver to extract the data from the sensor.

The IMU 3DM-GX3 -25 is a high-performance, miniature Attitude Heading Reference System (AHRS) using MEMS sensor technology. It combines a triaxial accelerometer, a triaxial gyro, a triaxial magnetometer, temperature sensors, and an on-board processor, running a sophisticated sensor fusion algorithm to provide static and dynamic orientation and inertial measurements. (the datasheet of the device is provided in Appendix A).

The laptop is a 64-bits Dell XPS M1330 with CPU Intel Core 2 Duo T5250 at 1.5 GHz with Data Bus Speed of 667 MHz.

The test layout and the used equipments are shown in Figure 4.1.

Figure 4.1: Experimental setup for the data acquisition.

As shown in Figure 4.1, the IMU was anchored to a vessel which was put inside a container with water to prevent the IMU to be sensitive to vibrations and other kind of environmental noise that could be added to the measured signals.

Three datasets with 9.5, 1, and 3 hours of gyros and accelerometers measurements were recorded, saved and exported to *.txt files. An example of the format of the output files is shown in Figure 4.2.

```
Computed gyro bias (x;y;z): = 0.001043793745; 0.004222712480; -0.010834034532

 Data corresponds to accelerations(x;y;z); gyro rates(x;y;z); time stamp
 Time stamp are nanoseconds from 1st Jan 1970
 Acceleration vector needs to be scaled by gravity modulus at measure location: 9.80261

0.157141372561; -0.085792757571; -0.987031161785; 0.002211321611; 0.000542887487; 0.000787906349; 1445776339557671000
0.157148823142; -0.085057221353; -0.985958039761; 0.002204418881; 0.002576438244; 0.000352729112; 1445776339567671000
0.157509967685; -0.084938399494; -0.985969305038; -0.003598247189; -0.000587796094; 0.002855019644; 1445776339577671000
0.157745912671; -0.085426256061; -0.986331641674; 0.001694442471; -0.001515156822; -0.005416879430; 1445776339587671000
0.156906262040; -0.085416853428; -0.985828042030; 0.006181766745; -0.005250370130; -0.001007677056; 1445776339597671000
0.156540662050; -0.086023531854; -0.986292302608; -0.001110073412; -0.001267342130; 0.007276295684; 1445776339607671000
0.156310692430; -0.084574960172; -0.986418247223; 0.000555657083; 0.002232763451; 0.004482892808; 1445776339617671000
0.156197682023; -0.083724334836; -0.985942542553; 0.005136832129; 0.001747120637; -0.003787890077; 1445776339627671000
0.156555846334; -0.084085874259; -0.985709607601; 0.002503974363; 0.001690430101; 0.001233174466; 1445776339637671000
0.156912237406; -0.084688827395; -0.985474646091; 0.004660217091; 0.000804894480; 0.002879807726; 1445776339647671000
0.157153800130; -0.084566868842; -0.985242605209; -0.002150794957; -0.000048187561; 0.004331198521; 1445776339657671000
0.156311556697; -0.084686927497; -0.985577523708; -0.000989954569; -0.004274911247; 0.005493270699; 1445776339667671000
0.156187713146; -0.085170395672; -0.985689818859; 0.001638111193; -0.001467610709; 0.000335480087; 1445776339677671000
0.155462190509; -0.085889659822; -0.985543012619; 0.001891689142; -0.000857714564; -0.001730904914; 1445776339687671000
```

Figure 4.2: Example of the format data recorded by the IMU.

In the files, the first three columns corresponds to the readings of the three accelerometers: accelerations in X,Y,Z axes expressed in gravities (g); the following three columns are the three

gyros measurements: rotation rates about its sensitive axes X,Y,Z expressed in radians per second (rad/s), and the last column corresponds to the time stamp in nanoseconds from 1970.

As the AVAR calculations and the error terms are expressed in m/s^2 for accelerations and degrees for the gyros, conversions of units from radians to degrees were carried out over all gyros data samples ($degrees = rad * 180/pi$) and from g to m/s^2 ($1g = 9.8m/s^2$) for all accelerometer data samples.

An example raw data reading has been plotted and it is shown in Figure 4.3. Analyzing the data, and because of the static positioning of the sensor, one may expect, ideally, a zero reading of angular rates and accelerations, except in the case of the accelerometer that is aligned with the gravity force, which is expected to have a nearly constant acceleration from gravity. In our case is the Z axis as it can be noticed in Figure 4.3.

The X,Y,Z gyro outputs are centered at zero value, but in the case of the X and Y accelerometers, their outputs are a bit off of zero, at 1.52 and -0.80 m/s^2, respectively. Probably the accelerometers are at a slight tilt with respect to the vector of Earth's gravity and they are therefore feeling a bit of the pull.

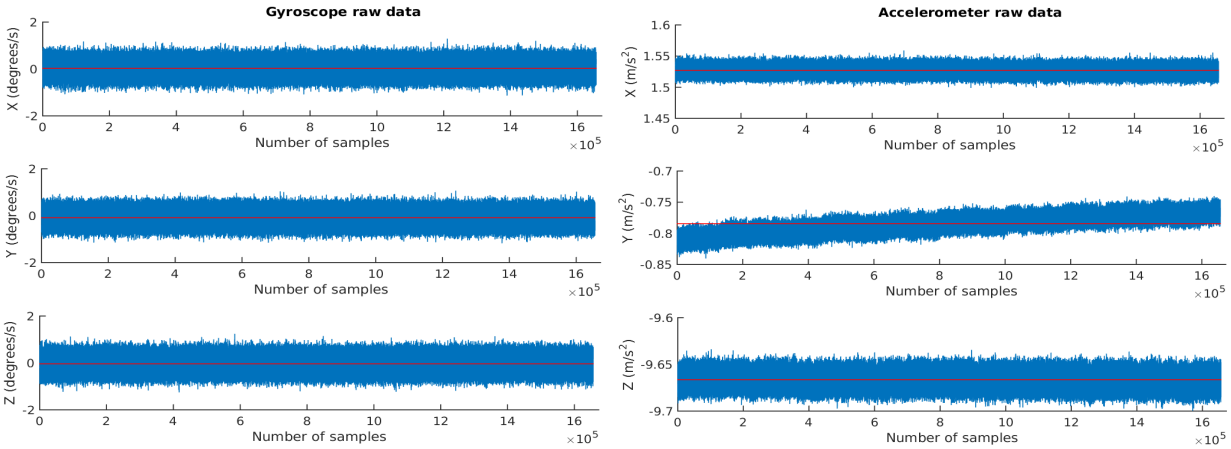

(a) (b)

Figure 4.3: (a) Gyros raw data, and (b)Accelerometers raw data for the three axes.

With the IMU at rest, the outputs should be zero, but there is always noise added on. The output might have a bias value, but it can be measured and subtract it out.

As shown in Figure 4.3, sometimes the noise takes the output above zero, and sometimes below, obtaining a range of values within a relatively thin spread. Noise is often thought of as the short-term variation in the output, such as the peak-to-peak output variation or the standard deviation of the output while the sensor is at rest. An issue in inertial sensors, that can be seen in a more accentuated way in the Y axis accelerometer, is the noise accumulated over the time.

4.2.1 Data preprocessing

As the Allan methodology involves calculations of variances, standard deviation and so on, a preprocessing of the data to prevent it from outliers causing false errors, was performed on all datasets that were used in the experiments.

A statistical outlier is an observation point distant from the rest of the observations, this may be due to variability in the measurement or it may indicate experimental errors.

To automatically detect the outliers a statistical approach is employed. The approach measures the spread of our data and marks the observations further from the center than usual. A good measure of spread is the interquartile range (IQR). IQR measures the statistical dispersion by subtracting the first quartile from the third quartile ($IQR = Q3 - Q1$).

With this information, the Tukey's test detects outliers as follows: the observations below $Q1 - F \times IQR$, or above $Q3 + F \times IQR$, are outliers for some nonnegative constant F. The value of F is set to 3 to detect "extreme" outliers, as proposed in [54]. The Figure 4.4 shows an example of the Boxplot for $F = 1.5$ (with an interquartile range) and a probability density function (pdf) of a Normal N $(0, \sigma 2)$ population.

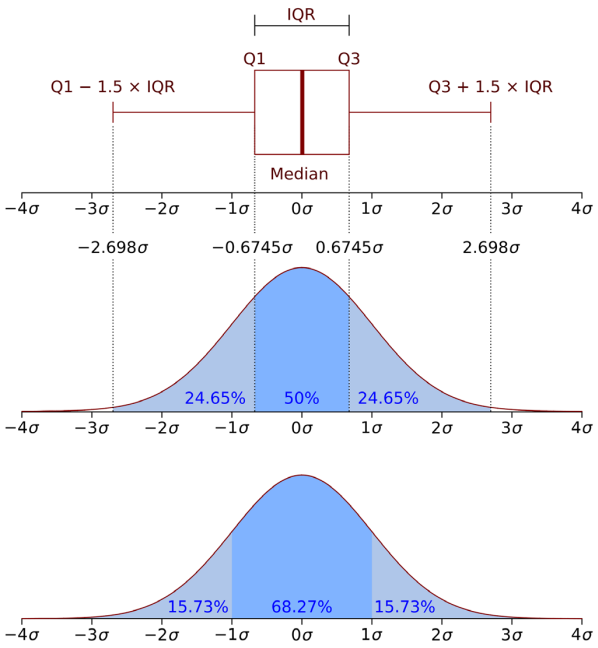

Figure 4.4: Example of a pdf for $F = 1.5$.

The Figure 4.5 shows an example of the process. The time series of the gyro in X axis (blue lines) and the boundaries $Q1 - 3 \times IQR$ and $Q3 + 3 \times IQR$ (horizontal red lines). As can be noticed, just one observation with value 0.024 is the above the upper boundary, this outlier is removed and replaced by the mean value of data.

After the preprocessing, all datasets are ready now to be used for the characterization of the 3DM-GX3-25 gyros and accelerometers.

4.3 AVAR implementation

The next step is to construct the Allan Deviation (σ) characteristic curves for their posterior analysis, in order to identify the error and noise terms affecting the sensors. The methodology and equations explained in Chapter 3 have been followed to develop the overlapping AVAR method under the Matlab environment (Appendix B).

The parameters set, the assumptions, principal equations and calculations that were used in the development of the AVAR, will be explained.

At this point we have the time domain signals from our sensors: a history of the sensors' output with N points of length in each dataset. For the study, three datasets of $N = 1.7 \times 10^6$, $N = 1.8 \times 10^5$ and $N = 6 \times 10^5$ number of samples, were utilized.

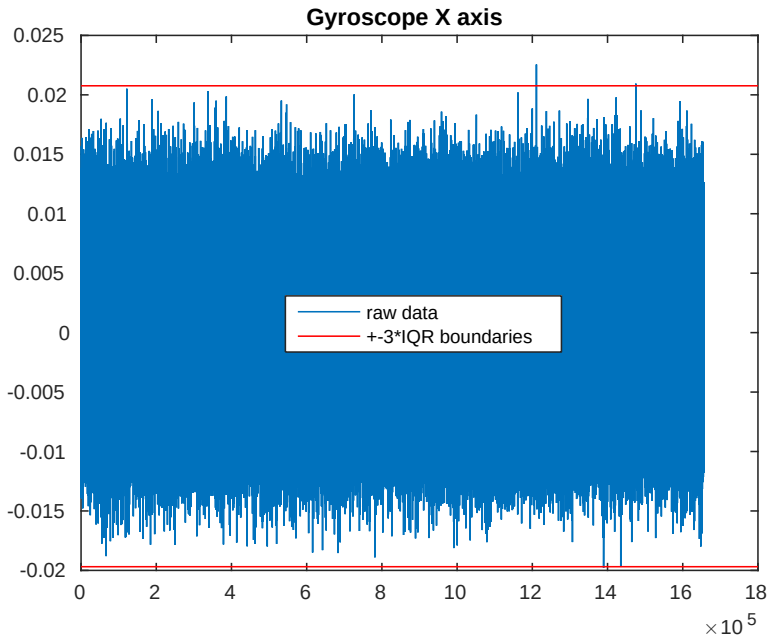

Figure 4.5: Example of data outliers removal.

From the number of samples and the time stamps provided by the sensors, the sampling rate $\tau_0 = 0.01s$ and sample frequency $f = 100$ Hz, were estimated.

The next step was to set the averaging factor m. As the value of m can be chosen arbitrarily fulfilling the condition $m < (N-1)/2$, a vector of log spaced numbers between 1 and $(N-1)/2$ values, was created. In this way, the averaging time or cluster time τ, is a vector with logarithmically spaced values, with $\tau = m * \tau_0$. The overlapping method to take the clusters is chosen to make maximum use of the dataset because it forms all possible overlapping sample clusters. The computation of the AVAR in terms of averages of output samples over each cluster was performed according to the equation 3.8, which is rewritten here as

$$\sigma^2(\tau) = \frac{1}{2\tau^2(N-2m)} \sum_{k=1}^{N-2m} (\theta_{k+2m} - 2\theta_{k+m} + \theta_k)^2. \tag{4.1}$$

where N is the total number of samples, m is the averaging factor, $\tau = m * \tau_0$ is the averaging time, and k is a set of discrete values varying from 1 to $N - 2m$.

For each τ value, the AVAR (σ^2) is calculated. From the square roots of AVAR values, the Allan Deviation (σ) value for each particular value of τ, is obtained. Iterations of the steps for the different and multiple values of τ provides us of the σ for each τ defined.

With $\sigma(\tau)$ values we are able to construct the Allan Deviation curve by plotting all the $\sigma(\tau)$ versus τ on a log-log plot.

Next figures show the obtained Allan standard deviation curves versus cluster time corresponding to one dataset ($N = 1.7 \times 10^6$), analyzed for the three axes gyros and the three axes accelerometers of the 3DM-GX3-25.

In the curves, the noises which oscillate quickly are found along the region with decreasing slopes due to the fact that in this part of the curves are the small cluster time frames, so the noise varies in less samples. In the regions of increasing slopes, the noise which oscillates over longer time frames begins to influence bigger groups of averaged data.

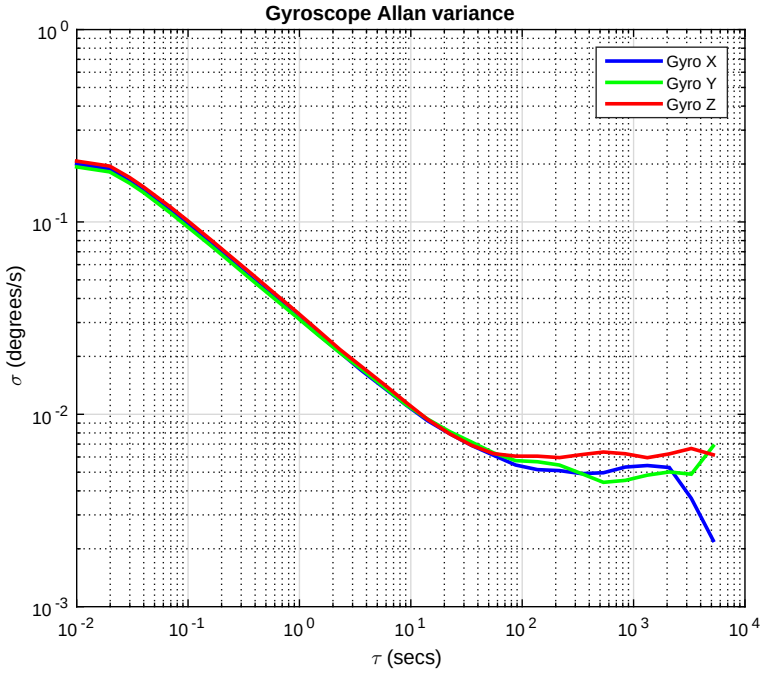

Figure 4.6: Three axes gyros Allan standard deviation.

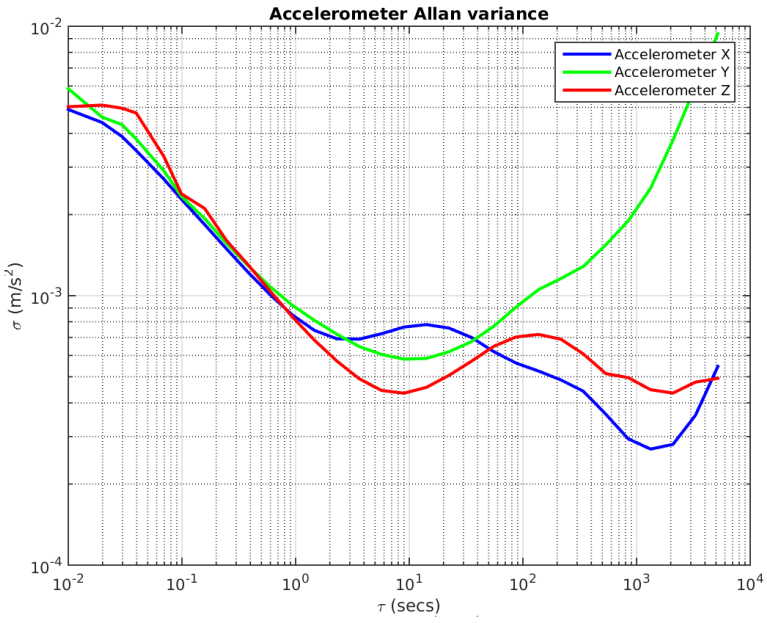

Figure 4.7: Three axes accelerometers Allan standard deviation.

Apart from noise types and values identification, the AVAR plots can bring a certain practical information about the IMU. For most of the applications in INS, in which is not necessary to take every sample reading, some averaging of the samples is done in order to provide a "final" output sample for the process of calculation. In those applications, and knowing that over enough time noise averages to zero, AVAR plots can be useful to see both averaging time and the number of samples to take in which the standard deviation of the data falls to its minimum, so a less quantity of noise is being taken.

As AVAR uses a log-log plot, it will give more weight to smaller numbers than larger numbers accentuating changes in the point of change that it will be the minimum group size in time and number o samples before the standard deviation start raising again.

4.3.1 Noise analysis

As stated in Chapter 3, from the inspection of some regions in the curves accomplishing some AVAR conditions, we are able to determine the different types and magnitude of noise terms existing in our sensors. Allan results are related to the five basic gyro-accelerometer noises: ARW/VRW, rate random walk, bias instability, quantization noise, and rate ramp.

As the majority of the noise terms are found by evaluating the slopes in specific regions in the curves, a process of finding the slopes were done by using the equation of a line, linear regression and derivatives, taking as a boundary points the τ vector values of the analyzed regions. The allowed error margin in the finding of the slopes were set from 0.01 to 0.015 in the Matlab code (Appendix B).

Gyros analysis

The two types of noise terms detected in the three axes gyros were the ARW and Bias Instability (BI). The other types of basic noise terms were not detected to be affecting the gyros.

Figure 4.8 shows an example of how to obtain the ARW and BI coefficients from the AVAR result in a log-log plot for X-axis gyro.

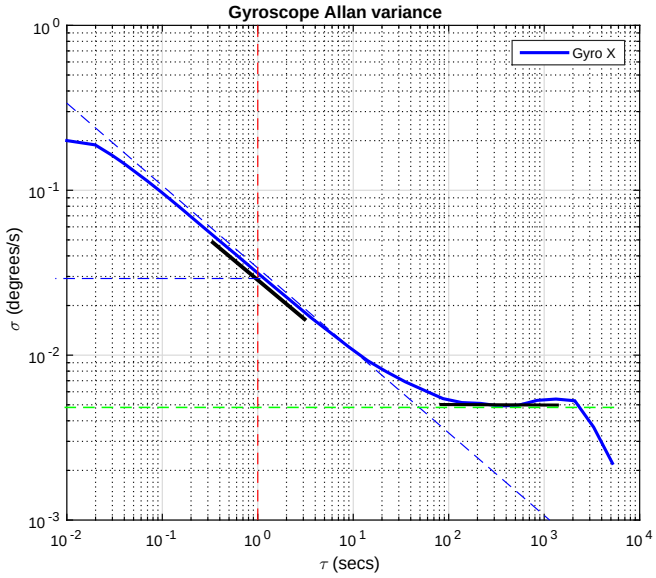

Figure 4.8: X axis gyro result.

In the region of the curve with slope -0.5 that intersects in $\tau = 10^0$s (1 second), the ARW value will be the corresponding σ at this point. A straight dashed line with slope of -0.5 was fitted to the curve for a better visualization of the interception point. The ARW is expressed in $^\circ/\sqrt{s}$.

Since the estimation of ARW is based on short cluster times, the number of independent clusters is large and the quality of estimation is good. Using equation 3.10, with $K = 100$ for all datasets since this noise is always found at 1 second, the percentage of error will only depends on the length of the datasets, the bigger datasets are the lower would be the estimation of error (more accuracy).

For the three axes gyros, using dataset 1, the error is about 0.54% ($N = 1.7 \times 10^6$); using dataset 2 the error of estimation is 1.5% ($N = 1.8 \times 10^5$) and in dataset 3 the error is about 1% ($N = 6 \times 10^5$).

The BI is found by looking for a flat area in the curve (slope 0) and picking up the minimum value of σ at that point. The value of this error can be measured with a flat line at σ value, and then dividing this standard deviation by the factor 0.664, as suggested in (IEEE Std 952-1997). The BI is expressed in $^\circ/h$.

The BI was also found in the 3 axes gyros, as Figure 4.9 shows. Since the estimation of BI is in the longer cluster times, the number of independent clusters is short and the quality of estimation is not so good as in the ARW. The BI were found at 500 seconds using dataset 1 and dataset 3, while for dataset 2 it was found at 100 seconds. The percentage of error of estimation of BI, using dataset 1 is about 17% for the three gyros, using dataset 2 the error is 35% for the three gyros, and using dataset 3 the estimation error is about 10% for the X gyro and about 23% for the Y and Z gyros.

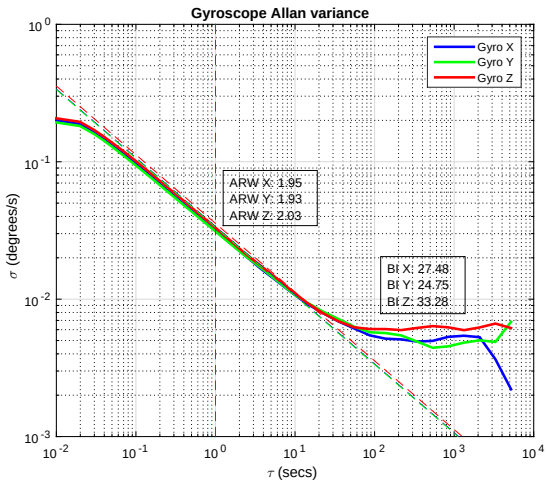

(a)

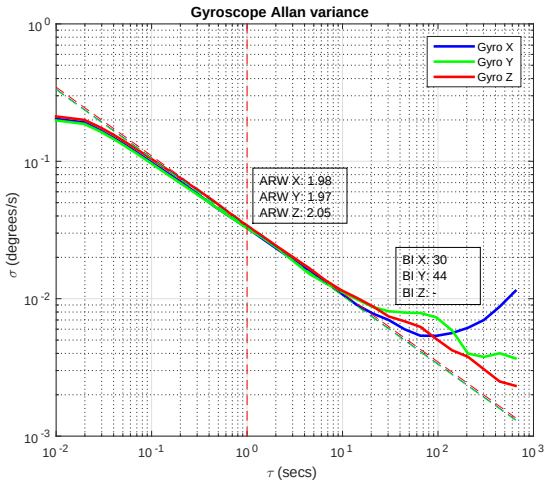

(b)

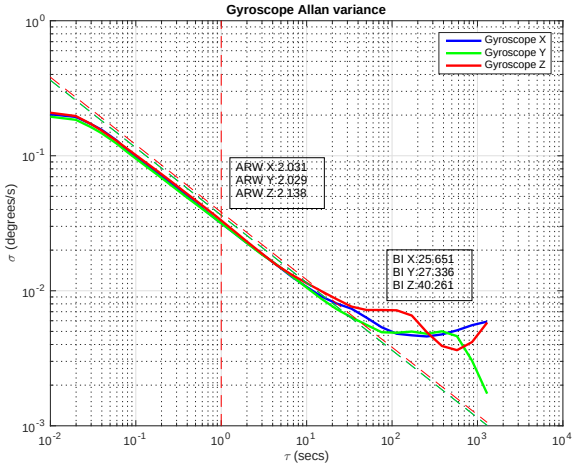

(c)

Figure 4.9: ARW and BI for gyros on (a) dataset 1, (b) dataset 2 and (c) dataset 3.

Figure 4.9 shows the values of the ARW and BI obtained for the three axes gyros using the different datasets. The curves show that the signal for the three gyros is mainly dominated by

short-term noises (high-frequency components), which are related to white noise and long term noises (low-frequency components).

Table 4.1 gathers the obtained values of ARW and BI in gyros.

Table 4.1: Noises values detected in 3 axis gyros.

Dataset 1	**ARW** $(^\circ/\sqrt{h})$	**BI** $(^\circ/h)$
Axis X	1.95 ± 0.01	27.48 ± 4.67
Axis Y	1.93 ± 0.009	24.75 ± 4.20
Axis Z	2.03 ± 0.01	33.28 ± 5.65
Dataset 2	**ARW** $(^\circ/\sqrt{h})$	**BI** $(^\circ/h)$
Axis X	1.98 ± 0.03	30 ± 9.00
Axis Y	1.97 ± 0.03	44 ± 13.20
Axis Z	2.05 ± 0.03	...
Dataset 3	**ARW** $(^\circ/\sqrt{h})$	**BI** $(^\circ/h)$
Axis X	2.03 ± 0.02	25.65 ± 2.50
Axis Y	2.02 ± 0.02	27.33 ± 6.28
Axis Z	2.13 ± 0.02	40.26 ± 9.25

The values of the ARW and the BI obtained are very similar in the three datasets for each axis gyro, so we may say that they are reliable enough. Although the bigger datasets have more accuracy on the estimations of the noise as stated before, an average of the results of all datasets equally weighted were done to provide the representative value of the noises in the three gyros.

- X gyro: $ARW = 1.98 \pm 0.01^\circ/\sqrt{h}$, and $BI = 31 \pm 5.4^\circ/h$.
- Y gyro: $ARW = 1.97 \pm 0.02^\circ/\sqrt{h}$, and $BI = 31.66 \pm 7.9^\circ/h$
- Z gyro:$ARW = 2.07 \pm 0.02^\circ/\sqrt{h}$, and $BI = 36.66 \pm 7.6^\circ/h$

Accelerometers analysis

Analyzing the AVAR plots for the three axes accelerometers, two noise terms were detected: the Velocity Random Walk (VRW) and BI.

The VRW are found in the Allan deviation plot in the same way as the ARW for the gyros (the corresponding σ if the curve has a slope of -0.5 at $\tau = 1s$). It is shown that its value is almost the same for all the three accelerometers. From the straight line with slope $-1/2$ fitted to the beginning of the VRW noise, a value of $0.05m/s/\sqrt{h}$at a cluster times of $1s$ can be read.

The inspection of the curve shows that the estimation of percentage error is very low in the region where the VRW is encountered . Using Equation 3.10 , for the dataset 1, dataset 2 and dataset 3, the estimation errors were about 0.5%, 1.5% and 1%, respectively.

The BI was encountered in the region of 10 seconds for the three axes in the three datasets ($K = 1000$, $K = \tau/\tau_0$), so the error when using dataset 1 is about 2.4%, for dataset 2 of 5%, and for dataset 3 is 3%.

Table 4.2 gathers the obtained values of the noises detected in the three accelerometers.

In the dataset 2 was not found VRW in X and Y axes accelerometers, but in the other two datasets, in the three axes, the value of the VRW obtained were exactly the same $0.005 \pm 0.00002m/s/\sqrt{h}$. In the case of the BI in each axis, the obtained values are very similar.

Thus, the obtained representative values of the noises detected in the three axis accelerometers are:

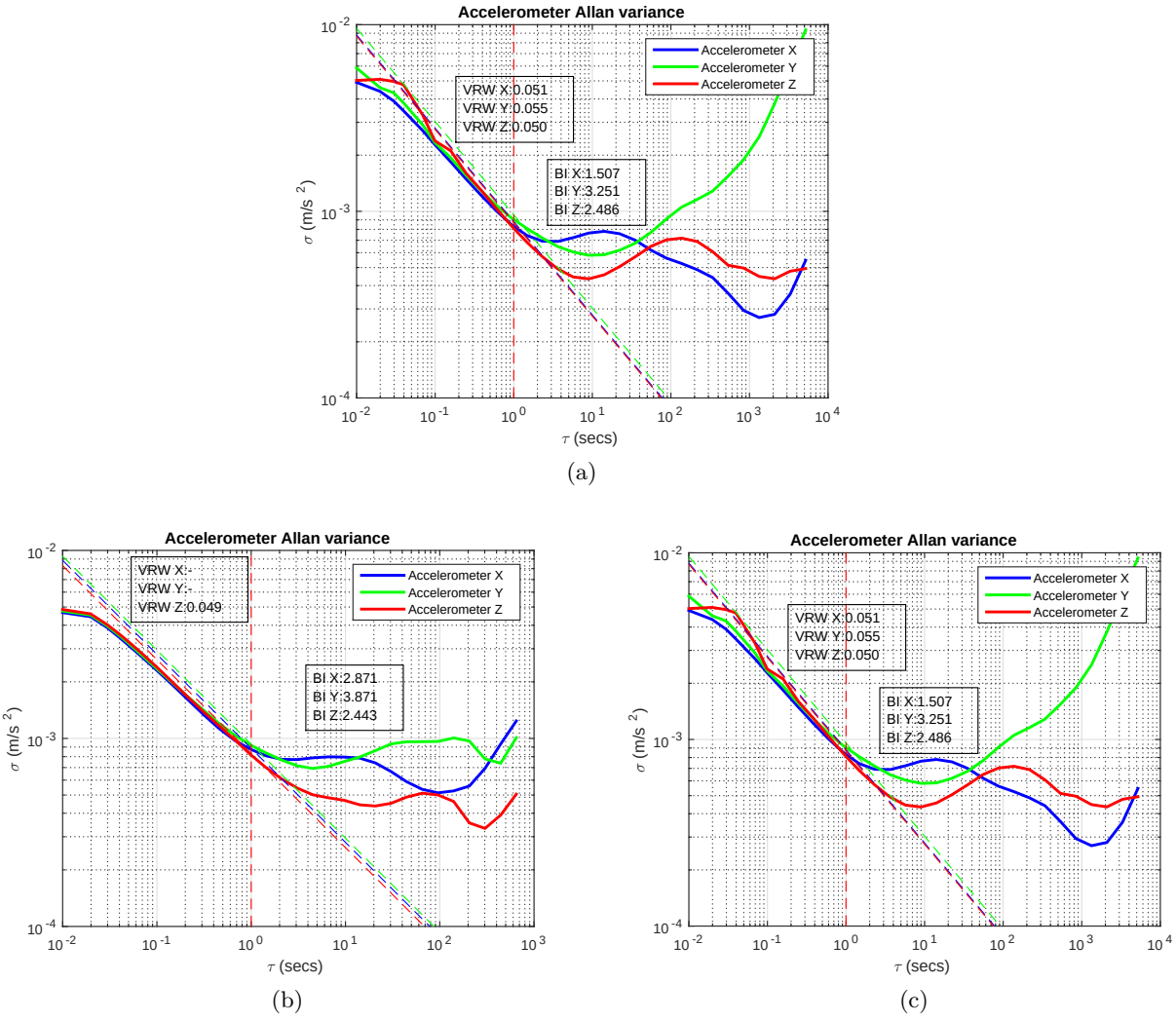

Figure 4.10: VRW and BI for accelerometers on (a) dataset 1, (b) dataset 2 and (c) dataset 3.

Table 4.2: Noises values detected in 3 axis accelerometers.

Dataset 1	**VRW** $(m/s/\sqrt{h})$	**BI** $(m/s/h)$
Axis X	0.005 ± 0.00002	1.50 ± 0.03
Axis Y	0.005 ± 0.00002	3.25 ± 0.07
Axis Z	0.005 ± 0.00002	2.48 ± 0.05
Dataset 2	**VRW** $(m/s/\sqrt{h})$	**BI** $(m/s/h)$
Axis X	...	2.87 ± 0.15
Axis Y	...	3.87 ± 0.20
Axis Z	0.005 ± 0.00007	2.44 ± 0.12
Dataset 3	**VRW** $(m/s/\sqrt{h})$	**BI** $(m/s/h)$
Axis X	0.005 ± 0.00005	2.57 ± 0.07
Axis Y	0.006 ± 0.00006	3.54 ± 0.10
Axis Z	0.005 ± 0.00005	2.53 ± 0.07

- X accelerometer: $VRW = 0.005 \pm 0.00003 m/s/\sqrt{h}$, and $BI = 2.31 \pm 0.08 m/s/h$.
- Y accelerometer: $VRW = 0.005 \pm 0.00003 m/s/\sqrt{h}$, and $BI = 3.55 \pm 0.12 m/s/h$.

- Z accelerometer: $VRW = 0.005 \pm 0.00003 m/s/\sqrt{h}$, and $BI = 2.48 \pm 0.08 m/s/h$.

At this point we have characterized the types and values of the noises affecting our gyros and accelerometers using the AVAR method. The obtained values have been compared with the obtained in [10] in which the IMU 3DM-GX3-25 was also utilized for a comparison between different error modeling of MEMS using AVAR and PSD. The values are very similar, so we can conclude that the methodology followed and the AVAR method are well suited for noise characterization.

4.4 Denoising

Once we have the knowledge about the noise types and values that are present in our sensor, the next step is to try to remove or reduce the affecting noise trough a denoising process. In digital signal processing there are different methods of noise reduction on a signal. The methods selected and applied in this work are the Discrete Wavelet Transform (DWT) and the Median Filter. Next sections show the obtained results of applying these two methods to the datasets. Both filters were applied to the data, and subsequently, processed with the AVAR algorithm in order to evaluate if the previously detected noises were removed or at least if their values has been reduced.

4.4.1 Wavelet denoising

The wavelet denoising process were performed using the Matlab Wavelet Toolbox. The Level of Decomposition (LoD) for the DWT and the wavelet family has been selected after the analysis of the reconstructed signal when applying different test values and parameters. In [55], some exhaustive procedures to select an optimal LoD, are explained.

From the several wavelet families two of them, Haar and Symlet8, were tested. Figure 4.11 shows how they return different reconstructed signals after filtering, and how the LoD impacts directly on the reconstruction wavelet.

Figure 4.11 depicts the AVAR standard deviation versus cluster times (τ) for the X-axis accelerometer after applying wavelet denoising with 4 , 8 and 12 LoD using Haar and Symlet8.

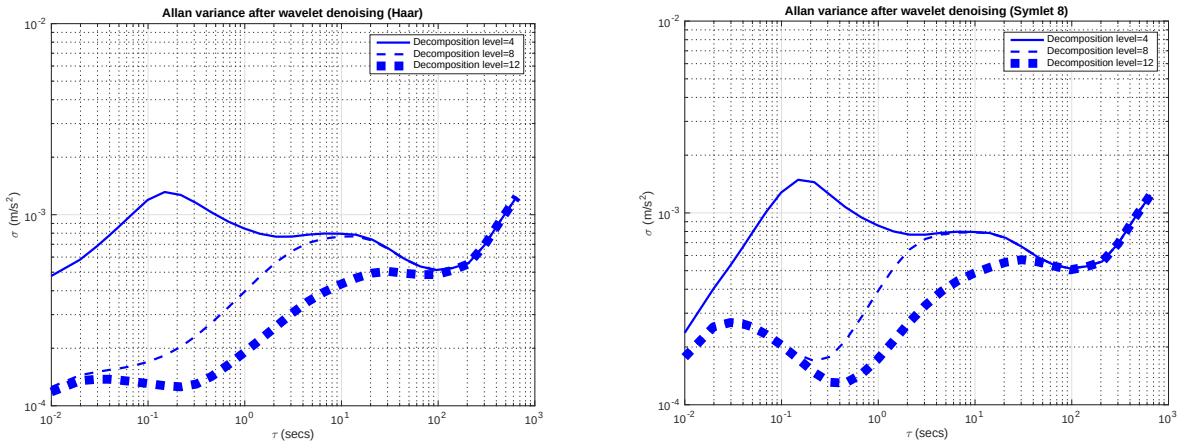

(a) (b)

Figure 4.11: X-axis accelerometer if IMU 3DM-GX-25 after applying wavelet denoising with 4, 8 and 12 levels of decomposition (a) A-Haar , (b) Symlet8.

According to this plot, it is noticed that the higher the LoD, the more high-frequency components are removed in both Haar and Symlet8. In the case of the low frequency components, they were only reduced using 12 LoD.

Thus, all the analysis will be done using 12 LoD and wavelet Symlet8 since not substantial difference is observed between Haar and Symlet 8 for our purposes.

Figure 4.12 shows the gyros and the accelerometers signals filtered, the blue signal is the raw data and the red one is the resulting signal after applying wavelets (using the dataset 1 as example). It is shown that,for gyros and accelometers, a big quantity of noise has been reduced.

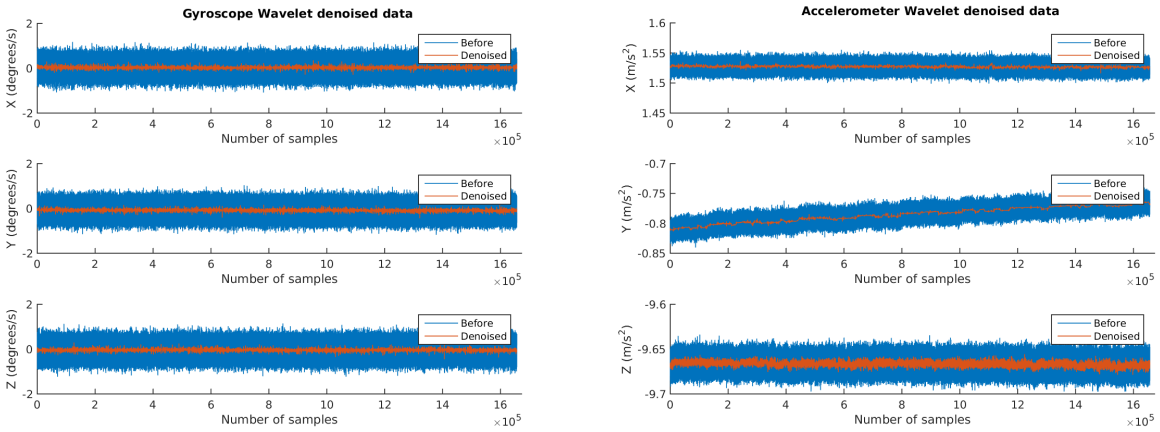

(a) (b)

Figure 4.12: Raw data and Wavelet filtered data in (a) gyros, and (b) accelerometers.

In the Figure 4.13a, the previously obtained AVAR plot without filtering, and the obtained AVAR after applying the wavelet denoising (Figures 4.13b 4.13c and 4.13d), are shown. It can be noticed that the wavelet denoising removed or reduced the short-term noises that were present in the AVAR original signal (ARW), while the long-term noises (BI) have been slightly attenuated.

The ARW was completely removed in the Y axis and highly reduced in the X and Z axes gyros from values of 1.95 to 0.10, and from 2.05 to 0.12, respectively . The BI was reduced in the three axis, from values of 27, 24 and 33 to 7, 8 and 7, respectively .

In dataset 2, the obtained AVAR plot shows that the ARW was removed in the three axes. The BI was slightly reduced in the three axes, from values of 30, 44 and 11 to 28, 12 and 14, respectively.

Table 4.3 gathers the obtained values before and after the denoising process for the gyros using the three datasets.

In a similar way, the analysis of the accelerometers are showed in Figure 4.14. As in the gyros, the wavelet denoising removed or reduced the VRW in a high accentuated way while reduced the BI in the three axes accelerometers.

Table 4.4 gathers the values of the noises obtained for the accelerometers.

4.4.2 Median filter denoising

As mentioned before, a median filter was also implemented in the process of denosing. The median filter is a simple filter and is based on replacing each observation by the median of the N-neighbouring observations [54] [55]. The N neighbours are called the "window". Hence, the resulting signal will depend directly on the parameter N selected. In particular, we set $N = 20$

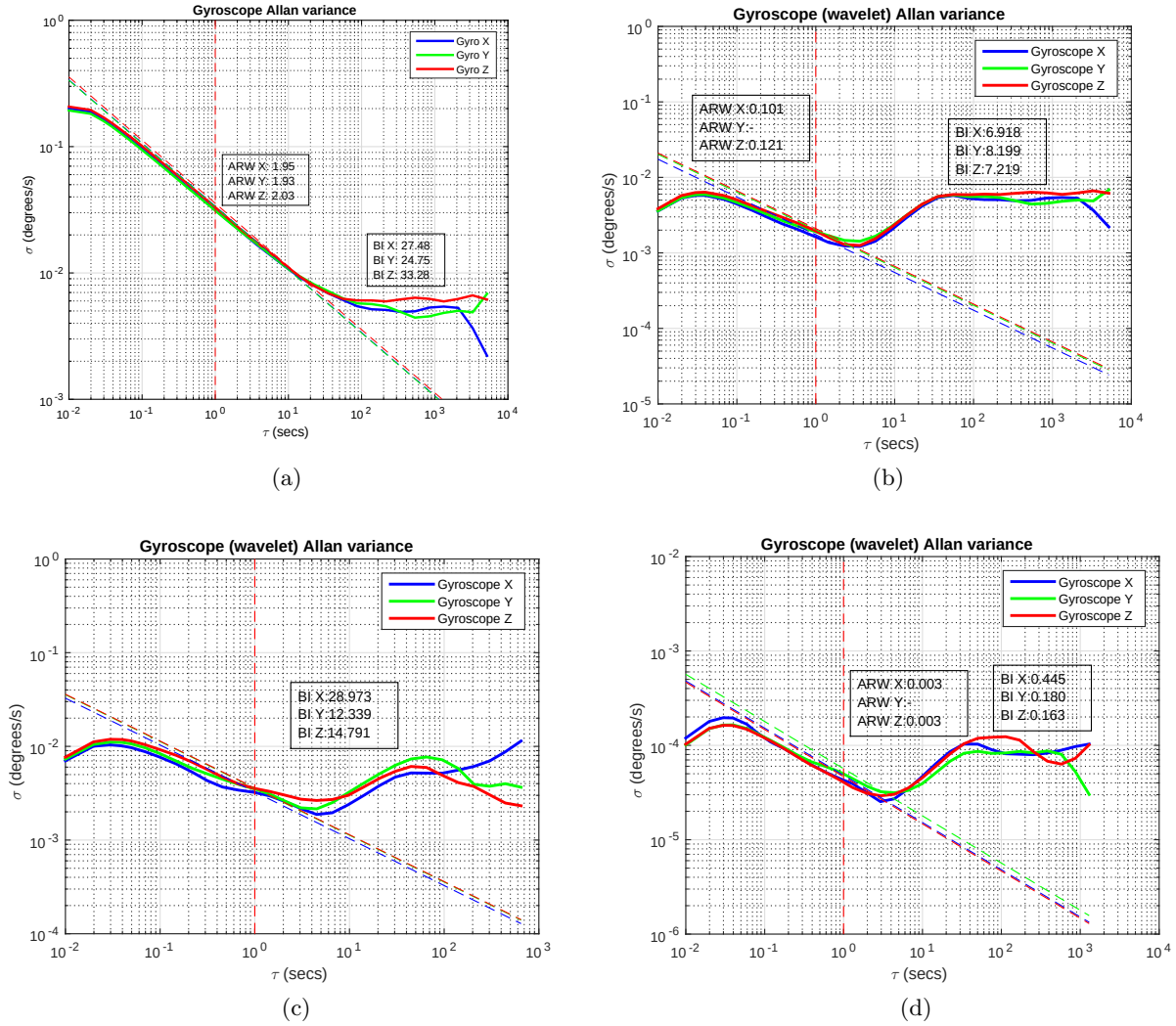

Figure 4.13: Three axes gyros AVAR analysis, (a) dataset 1 without filtering (comparison purposes), (b) dataset 1 filtered with wavelets , (c) dataset 2 filtered with wavelets, (d) dataset 3 filtered with wavelets.

Table 4.3: Noises values detected in 3 axis gyros with and without Wavelet denoising.

Dataset 1	**ARW**) $(^\circ/\sqrt{h})$	**ARW (denoised)** $(^\circ/\sqrt{h})$	**BI** $(^\circ/h)$	**BI (denoised)** $(^\circ/h)$
Axis X	1.95 ± 0.01	0.10	27.48 ± 4.67	6.91
Axis Y	1.93 ± 0.009	...	24.75 ± 4.20	8.19
Axis Z	2.03 ± 0.01	0.12	33.28 ± 5.65	7.21
Dataset 2	**ARW** $(^\circ/\sqrt{h})$	**ARW (denoised)** $(^\circ/\sqrt{h})$	**BI** $(^\circ/h)$	**BI (denoised)** $(^\circ/h)$
Axis X	1.98 ± 0.03	0	30 ± 9.00	28.97
Axis Y	1.97 ± 0.03	0	44 ± 13.20	12.33
Axis Z	2.05 ± 0.03	0	...	...
Dataset 3	**ARW** $(^\circ/\sqrt{h})$	**ARW (denoised)** $(^\circ/\sqrt{h})$	**BI** $(^\circ/h)$	**BI (denoised)** $(^\circ/h)$
Axis X	2.03 ± 0.02	0.15	25.65 ± 2.50	25.49
Axis Y	2.02 ± 0.02	0	27.33 ± 6.28	10.32
Axis Z	2.13 ± 0.02	0.14	40.26 ± 9.25	9.35

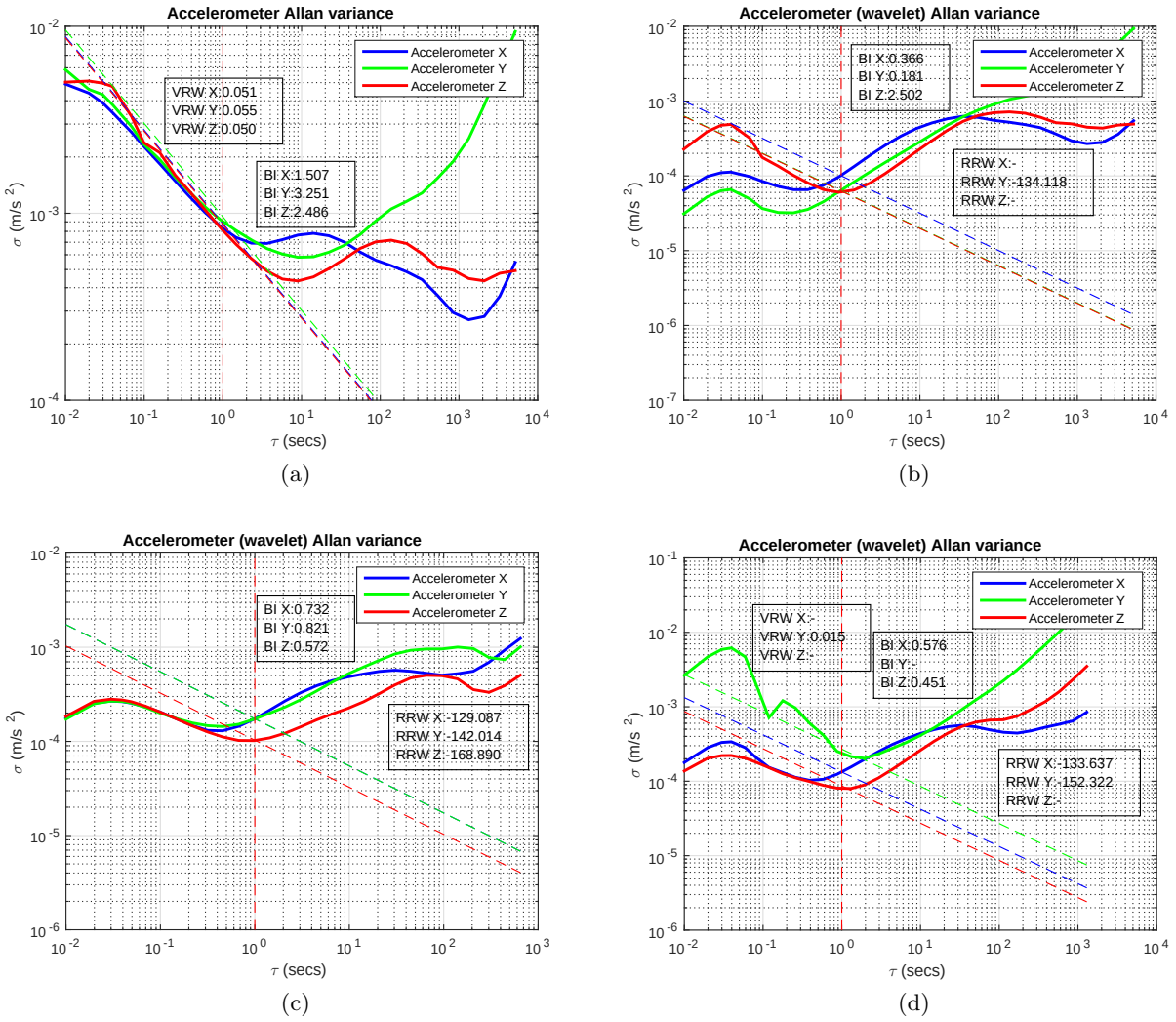

Figure 4.14: Three axes accelerometers AVAR analysis, (a) dataset 1 without filtering (comparison purposes), (b) dataset 1 filtered with wavelets , (c) dataset 2 filtered with wavelets, (d) dataset 3 filtered with wavelets.

Table 4.4: Noises values detected in 3 axis acceleremoter with and without Wavelet denoising.

Dataset 1	**VRW**) $(m/s/\sqrt{h})$	**VRW (denoised)** $(m/s/\sqrt{h})$	**BI** $(m/s/h)$	**BI (denoised)** $(m/s/h)$
Axis X	0.005 ± 0.00002	0	1.50 ± 0.03	0.36
Axis Y	0.005 ± 0.00002	0	3.25 ± 0.07	0.18
Axis Z	0.005 ± 0.00002	0	2.48 ± 0.05	2.50
Dataset 2	**VRW** $(m/s/\sqrt{h})$	**VRW (denoised)** $(m/s/\sqrt{h})$	**BI** $(m/s/h)$	**BI (denoised)** $(m/s/h)$
Axis X	...	...	2.87 ± 0.15	0.73
Axis Y	...	...	3.87 ± 0.20	0.82
Axis Z	0.005 ± 0.00007	0	2.44 ± 0.12	0.57
Dataset 3	**VRW** $(m/s/\sqrt{h})$	**VRW (denoised)** $(m/s/\sqrt{h})$	**BI** $(m/s/h)$	**BI (denoised)** $(m/s/h)$
Axis X	0.005 ± 0.00005	0	2.57 ± 0.07	0.57
Axis Y	0.006 ± 0.00006	0.015	3.54 ± 0.10	0
Axis Z	0.005 ± 0.00005	0	2.53 ± 0.07	0.45

for the results presented in this work, as it was the maximum value that the PC performace could afford.

As can be notice from Figure 4.15, analyzing the filtered signal, not too much noise were removed comparing with the wavelet filtering.

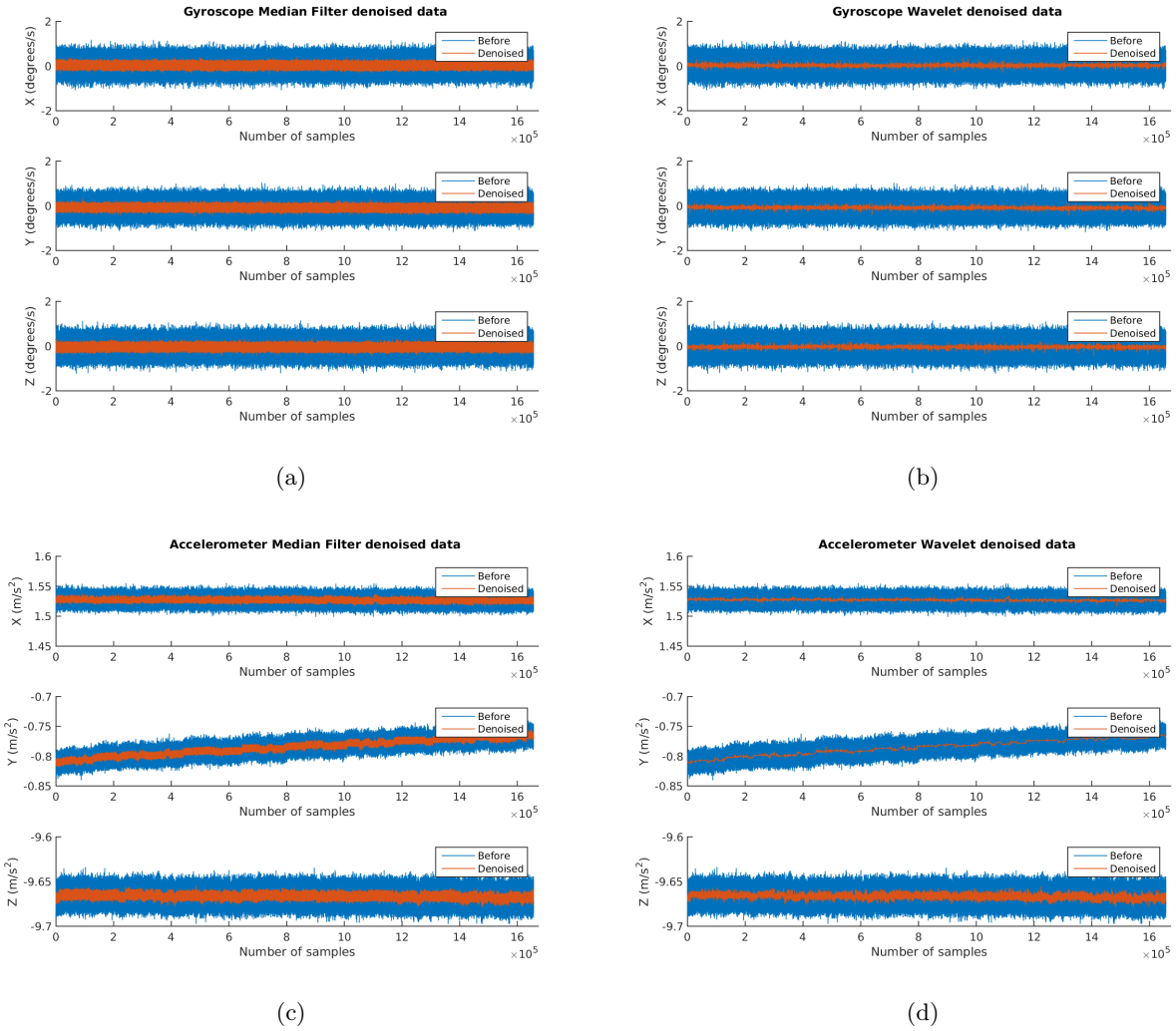

Figure 4.15: (a) dataset 1 gyros noise filtered with Median Filter, (b) dataset 1 gyros noises filtered with Wavelets, (c) dataset 1 accelerometers noises filtered with Median Filter, (d) dataset 1 accelerometers noises filtered with Wavelets.

Figure 4.16 shows the AVAR plots for the gyros and accelerometers filtered with the Median Filter using dataset 1. The ARW in the gyros were not attenuated, on the contrary, the values are a little bit higher or almost the same. The values of the BI are also almost the same before and after filtering. In the accelerometers, the VRW was removed in the X and Y axes, and in the Z axis the value before and after filtering was the same $0.05m/s/\sqrt{(h)}$. The BI in the accelerometers increase a little bit its value.

Using dataset 2 and dataset 3, the obtained results are very similar to the stated before.

Next tables gather the obtained values using all datasets.

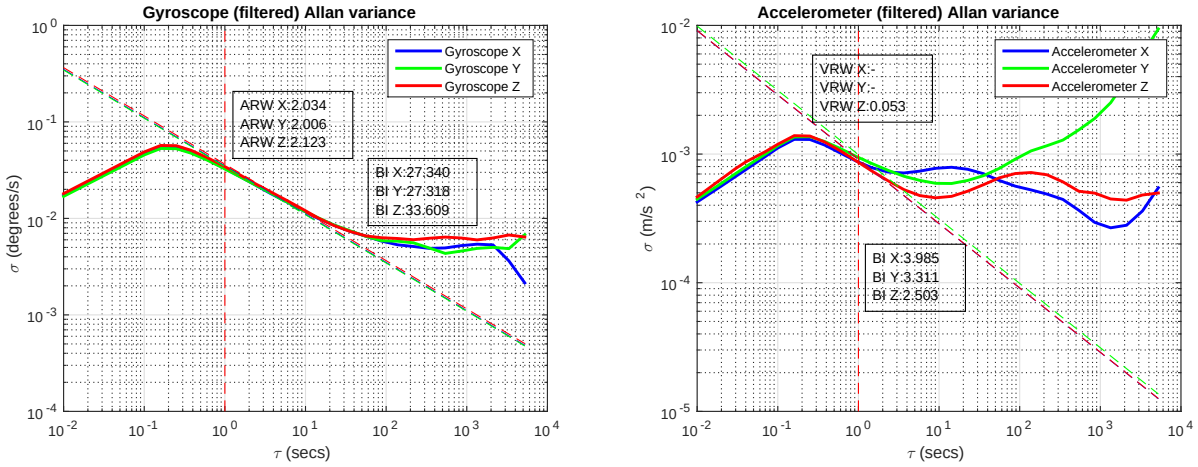

(a) (b)

Figure 4.16: (a) dataset 1 gyros noises filtered with Median Filter, (b) dataset 1 accelerometers noises filtered with Median Filter.

Table 4.5: Noises values detected in 3 axis gyros with and without Median Filter denoising.

Dataset 1	**ARW**) $(°/\sqrt{h})$	**ARW (Median Filter)** $(°/\sqrt{h})$	**BI** $(°/h)$	**BI (Median Filter)** $(°/h)$
Axis X	1.95 ± 0.01	2.03	27.48 ± 4.67	27.34
Axis Y	1.93 ± 0.009	2.00	24.75 ± 4.20	27.31
Axis Z	2.03 ± 0.01	2.12	33.28 ± 5.65	33.60
Dataset 2	**ARW** $(°/\sqrt{h})$	**ARW (Median Filter)** $(°/\sqrt{h})$	**BI** $(°/h)$	**BI (Median Filter)** $(°/h)$
Axis X	1.98 ± 0.03	2.04	30 ± 9.00	30.80
Axis Y	1.97 ± 0.03	2.05	44 ± 13.20	18.62
Axis Z	2.05 ± 0.03	2.15	...	...
Dataset 3	**ARW** $(°/\sqrt{h})$	**ARW (Median Filter)** $(°/\sqrt{h})$	**BI** $(°/h)$	**BI (Median Filter)** $(°/h)$
Axis X	2.03 ± 0.02	2.08	25.65 ± 2.50	31.35
Axis Y	2.02 ± 0.02	2.10	27.33 ± 6.28	27.88
Axis Z	2.13 ± 0.02	2.21	40.26 ± 9.25	40.52

Table 4.6: Noises values detected in 3 axis acceleremoter with and without Median Filter denoising.

Dataset 1	**VRW**) $(m/s/\sqrt{h})$	**VRW (Median Filter)** $(m/s/\sqrt{h})$	**BI** $(m/s/h)$	**BI (Median Filter)** $(m/s/h)$
Axis X	0.005 ± 0.00002	0	1.50 ± 0.03	3.98
Axis Y	0.005 ± 0.00002	0	3.25 ± 0.07	3.31
Axis Z	0.005 ± 0.00002	0.05	2.48 ± 0.05	2.50
Dataset 2	**VRW** $(m/s/\sqrt{h})$	**VRW (Median Filter)** $(m/s/\sqrt{h})$	**BI** $(m/s/h)$	**BI (Median Filter)** $(m/s/h)$
Axis X	...	...	2.87 ± 0.15	2.87
Axis Y	...	...	3.87 ± 0.20	4.02
Axis Z	0.005 ± 0.00007	0.05	2.44 ± 0.12	2.49
Dataset 3	**VRW** $(m/s/\sqrt{h})$	**VRW (Median Filter)** $(m/s/\sqrt{h})$	**BI** $(m/s/h)$	**BI (Median Filter)** $(m/s/h)$
Axis X	0.005 ± 0.00005	0	2.57 ± 0.07	2.56
Axis Y	0.006 ± 0.00006	0	3.54 ± 0.10	3.97
Axis Z	0.005 ± 0.00005	0.05	2.53 ± 0.07	2.64

Chapter 5

Conclusions

This Thesis work has addressed the problems of characterizing and identifying the noises inherent to inertial sensors as gyros and accelerometers, which are embeeded in inertial navigation systems. The proper weighting of these noise values habilitates the calibration of IMUs, which are devices that provide position information about the platform on which they are mounted by combining multi axes gyros and accelerometers. This procedure allows having more accurate tracking systems, which are key in several applications as unmanned vehicles,inertial aiding of GPS, computer science, aircraft and spacecraft positioning, robotics and other militar and industrial applications.

To achieve this goal, a deep study of the different gyros and accelerometers existing in literature, has been carried out. The basic working principles, different types, characteristics, and trend of these inertial sensors have been reviewed, hightlighting the MEMS technology due to its excellent relation between cost and benefits.

Also an analysis of the Allan variance method to characterize and identify the noises related to these sensors, has been done. Several noises have been clasified to affect these sensors, and the way as the Allan variance, along with the power spectral density, deal with them, is studied. In addition, a denoising process based in the Wavelet transform is analyzed and its benefits clearly established.

The practical implementation of the AVAR method for the noises characterization has been performed over an experimental setup based on an IMU which is positioned in a stable rest position, and an acquisition of its output data is done. Three datasets are collected, and a preprocessing step is done to remove outliers from the data. Once the data is outliers-free, an AVAR method is done, by coding the method in Matlab. From the AVAR plots it is possible to identify the main types of noises present in the sensors, ARW and Bias instability for gyros, and VRW and BI for accelerometers, as well as their values. A denoising process is also performed by the use of Wavelet transform, which is coded using the Wavelet Toolbox of Matlab. As it could be observed, better results are obtained using this technique, improving the results of the AVAR. In the contrary, the Median Filter was also used to observe its performance, giving a poor behaviour.

It is possible to conclude that the objective of the Thesis was accomplished. A simple tool, based in AVAR plus Wavelet denoising, is developed. This tool is very simple and provides excellent results, and was used in an experimental setup. It was also compared against other results in literature, obtaining excellent agreements.

It would be interesting to study other filters to observe their denoising perfomance, in order to gain accuracy in the MEMS sensors measurements. This will address even more the use of this kind

of sensors in high accuracy applications. This, along with their compact form, easy integration, and their low costs, will turn the IMU MEMS based technology in the dominant one in the future.

List of Figures

List of Tables

Bibliography

[1] D. H. Titterton and J. L. Weston, *Strapdown Inertial Navigation Technology.* The Institution of Electrical Engineers, 2004. [cited at p. 3, 8, 9, 11, 12, 13, 16, 17, 19, 53]

[2] O. J. Woodman, "An introduction to inertial navigation," University of Cambridge, UCAM-CL-TR-696, ISSN 1476-2986, Tech. Rep., 2007. [cited at p. 3]

[3] O. Duran, K. Althoefer, and l. D. Seneviratne, "State of the art in sensor technologies for sewer inspection," *IEEE Sensors Journal, Vol. 2, No. 2, pp. 73-81,*, 2002. [cited at p. 3]

[4] "Guide to comparing gyro and IMU technologies micro-electro-mechanical systems and fiber optic gyros," KVH Industries, Tech. Rep., 2014. [cited at p. 3, 8, 12]

[5] C. Aszkler, *Acceleration, Shock and Vibration Sensors*, J. S. Wilson, Ed. Sensor Technology Handbook, Elsevier, 2005. [cited at p. 3]

[6] A. Lawrence, *Modern Inertial Technology: Navigation, Guidance, and Control.* Springer, 1993. [cited at p. 4, 11]

[7] P. H. Savet, *Gyroscopes: theory and design.* MacGraw-Hill, 1961. [cited at p. 4, 8, 9]

[8] R. G. Brown, *Introduction to Random Signal Analysis and Kalman Filtering*, I. John Wiley & Sons, Ed., 1983. [cited at p. 4]

[9] S. M. Grewal and A. P. Andrews, *Kalman Filtering Theory and Practice*, P. Hall., Ed. Uppe r Saddle River, NJ USA, 1993. [cited at p. 4]

[10] A. Quinchia, G. Falco, E. Falleti, F. Dovis, and C. Ferrer, "A comparison between different error modeling of MEMS applied to GPS/INS integrated systems," *Sensors, pp. 9549-9588*, 2013. [cited at p. 4, 45]

[11] D. Allan, "Statistics of atomic frequency standards," *Proceedings of the IEEE , Vol. 54 , Is. 2, pp. 221-230*, 1966. [cited at p. 4, 25]

[12] H. Hou and N. El-Sheimy, "Inertial sensors errors modelling using Allan Variance," *Proceedings of ION GNSS 2003*, 2003. [cited at p. 4, 21, 25]

[13] N. El-Sheimy, H. Haiying, and N. Xiaoji, "Analysis and modeling of inertial sensors using Allan variance," *IEEE Transactions on Instrumentation and Measurement, Vol. 57, No. 1*, 2008. [cited at p. 4, 21, 26, 27, 28, 29]

[14] R. Cohen, "Signal denoising using wavelets," Department of Electrical Engineering Technion, Israel Institute of Technology, Tech. Rep., 2012. [cited at p. 4, 33]

[15] T. Park, "An introduction to wavelets and wavelet de-noising," Lancaster University, Tech. Rep., 2011. [cited at p. 4, 33]

[16] S. Merlo, M. Norgia, and S. Donati, *Handbook of Fibre Optic Sensing Technology, Chapter 16: Fiber Giroscope Principles.* John Wiley & Sons Ltd, 2000. [cited at p. 8, 18]

[17] "Rate integrating gyroscope (RIG) . the RIG, revisited (Part I)," US Dynamics Corp, Tech. Rep., 2007. [cited at p. 8]

[18] R. J. G. Craig, "Theory of operation of an elastically supported tuned gyroscope," *IEEE Transactions on Aerospace and Electronic System, AES-8 (3), pp. 280-297*, 1972. [cited at p. 8]

[19] A. Trusov, A. Schofield, and A. Shkel, "Micromachined rate gyroscope architecture with ultra-high quality factor and improved mode ordering," *Sens. Actuators A: Phys. , pp. 2634*, 2010. [cited at p. 8]

[20] B. Johnson and I. M. Longden, "Vibrating structure gyroscopes and their applications," in *DGON Proceedings, Gyro Technology Symposium, Stuttgart*, 1994. [cited at p. 8]

[21] A. . M. Shkel, "Type I and type iI micromachined vibratory gyroscopes," in *Proc. IEEE/ION Position Locat. Navigat. Symp. , San Diego, CA, pp. 586-593,*, 2006. [cited at p. 8]

[22] A. A. Trusov, I. P. Prikhodko, S. A. Zotov, and A. M. Shkel, "Low-dissipation silicon tuning fork gyroscopes for rate and whole angle measurements," *IEEE Sensors Journal, Vol. 11, No. 11, pp. 2763-2770*, 2011. [cited at p. 8]

[23] L. Xie, X. Wu, S. Li, H. Wang, J. Su, and P. Dong, "A Z-Axis quartz cross-fork micromachined gyroscope based on shear stress detection," *Sensors, Vol.10, pp. 1573-1588,*, 2010. [cited at p. 8]

[24] A. Trusov, I. Prikhodko, S. Zotov, A. Schofield, and A. Shkel, "Ultra high Q silicon gyroscopes with interchangeable rate and whole angle modes of operation," in *Proc. IEEE Sensors Conf. , Waikoloa, pp. 864867,*, 2010. [cited at p. 9]

[25] F. A. Karwacki, "Nuclear magnetic resonance gyro development," in *Navigation Journal of the Institute of Navigation, 27 (1)*, 1980. [cited at p. 9]

[26] E. Kanegsburg, "A nuclear magnetic resonance (NMR) gyroscope with optical magnetometer detection," in *SPIE 157, Laser Inertial Rotation Sensors, 73*, 1978. [cited at p. 9]

[27] T. J. Kaiser and M. G. Allen, "A micromachined pendulous oscillating gyroscopic accelerometer," in *Solid-State Sensor and Actuator Workshop Hilton Head Island, South Carolina, USA.*, 2000. [cited at p. 11]

[28] G. Sagnac, "L' ether lumineux demonstre par l'effet du vent relatif d'ether dans un interferometre en rotation uniforme," *Comptes Rendus de l'Academie des Sciences, 157, p. 708*, 1913. [cited at p. 11]

[29] P. R. Aywarya, S. S. Pournami, and R. Nambiar, "A survey on ring laser gyroscope technology," *International Journal of Computer Applications, Vol. 116, No. 2*, 2015. [cited at p. 12]

[30] V. Sahu, S. Kumar, and R. Kumar, "Laser and fiber-optic gyro: The satus and tendencies of developments," *International Journal of Innovative Research in Technology, Vol. 1, Iss. 6, pp. 1618-1622*, 2014. [cited at p. 12]

[31] A. Kersey, "Fiber optic gyroscope technology," *Optics News, pp. 12-19*, 1989. [cited at p. 13, 53]

[32] M. N. Armenise, C. Ciminelli, F. Dell'Olio, and V. M. N. Passaro, *Advances in Gyroscopes Technologies.* Springer, 2010. [cited at p. 14, 18, 53]

[33] W. Bernard, R. Englert, R. Fangmeier, E. Froning, K. Langner, and K. Schwarz, "Waveguide ring resonators in glass for optical gyros," in *DGON Proceedings, Gyro Technology Symposium, Stuttgart*, 1986. [cited at p. 15]

[34] D. L. D. Uttamchandani and B. Culshaw, "A micromachined silicon accelerometer with fiber optic integration." *In Proc. SPIE Integrated Optics and Microstructures, vol. 1793, pp. 2733*, 1992. [cited at p. 16]

[35] J. M. et al., "Fiber-optic accelerometer using silicon micromachined techniques," *Sensors and Actuators A, vol. 46-47, pp. 470-473,*, 1995. [cited at p. 16]

[36] K. P. Zetie, S. F. Adams, and R. M. Tocknell, "How does a machzehnder interferometer work?" *Phys. Educ. 35 (1), pp. 46-48*, 2000. [cited at p. 16]

[37] W. B. Spillman, *Fiber Optic Sensors: An Introduction for Engineers and Scientists, Chapter 10*, E. Udd, Ed. Wiley, 2011. [cited at p. 16]

[38] K. Hill, Y. Fujii, D. C. Johnson, and B. S. Kawasaki, "Photosensitivity in optical fiber waveguides: Application to reflection fiber fabrication," *Appl. Phys. Lett. 32 (10): pp. 647*, 1978. [cited at p. 16]

[39] D. Lynch, "Coriolis vibratory gyros," in *Proc. Symp. Gyro Technol. , Stuttgart, pp. 1.0-1.14,*, 1998. [cited at p. 18]

[40] J. Esfandyari, R. D. Nuccio, and G. Xu, "Introduction to MEMS gyroscopes," STMicroelectronics, Tech. Rep., 2010. [cited at p. 18, 53]

[41] A. M. Lestev and M. V. Fedorov, "Vibration-induced error of a pendulous MEMS accelerometer," *Gyroscopy and Navigation, Vol. 3, Iss. 1, pp 47-50*, 2012. [cited at p. 19]

[42] O. R. H. et. al., "Post-CMOS-compatible aluminum nitride resonant MEMS accelerometers," *Journal of Microelectromechanical Systems, Vol. 18, No. 3, pp. 671-678*, 2009. [cited at p. 19]

[43] C. H. Liu and T. W. Kenny, "A high-precision, wide-bandwidth micromachined tunneling accelerometer," *Journal of Microelectromechanical Systems, Vol. 10, No. 3, pp. 425-433*, 2001. [cited at p. 20]

[44] H. Haiying, "Modeling inertial sensors errors using Allan variance," Ph.D. dissertation, University of Calgary, (URL: http://www.geomatics.ucalgary.ca/links/GradTheses.html), 2004. [cited at p. 21, 22, 27, 28, 32, 33]

[45] W. Stockwell, "Angle random walk," Crossbow Technology, Inc., Tech. Rep., 2000. [cited at p. 21]

[46] C. N. Lawrence, "On the application of Allan variance method for ring laser gyro performance characterization," Lawrence Livermore National Laboratory, Tech. Rep., 1993. [cited at p. 22, 25, 28, 29, 31, 32, 33, 53]

[47] J. R. Gilbert, "Exploring design spaces for optical MEMS devices," in *Advanced Applications of Lasers in Materials Processing, IEEE/LEOS Summer Top. Meet., 5-9, pp. 54 55*, 1996. [cited at p. 23]

[48] N. El-Sheimy and X. Niu, "The promise of MEMS to the navigation community," *Inside GNSS, pp. 4656.*, 2007. [cited at p. 23]

[49] N. El-Sheimy, S. Nassar, and A. Noureldin, "Wavelet de-noising for imu alignment," *IEEE Aerosp. Electron. Syst. Vol. 19, pp. 3239.*, 2004. [cited at p. 25]

[50] J. Skaloud, A. M. Bruton, and K. P. Schwarz, "Detection and filtering of short-term (1/f) noise in nertial sensors," *NAVIGATION: Journal of The Institute of Navigation, Vol. 46, No 2, Summer 1999, pp. 97-107*, 1999. [cited at p. 25]

[51] N. El-Sheimy, S. Nassar, K. P. Schwarz, and A. Noureldin, "Modeling inertial sensor errors using autoregressive (AR) models," *Navigation, Vo. 51, Iss. 4, pp. 259268*, 2004. [cited at p. 25]

[52] M. Marinov and Z. Petrov, "Allan variance analysis on error characters of low-cost MEMS accelerometer MMA8451Q," in *International Conference of Scientific Paper AFASES 2014*, 2014. [cited at p. 26, 53]

[53] R. Cohen, "Signal denoising using wavelets," Department of Electrical Engineering Technion, Israel Institute of Technology, Tech. Rep., 2012. [cited at p. 32]

[54] W. K. Pratt, *Digital Image Processing*, N. 4th Ed. Hoboken, Ed. John Wiley & Sons, 2007. [cited at p. 38, 46]

[55] S. W. Smith, *The Scientist & Engineer's Guide to Digital Signal Processing*, 1st Ed. California Technical Pub, Ed., 1997. [cited at p. 45, 46]

Appendices

Appendix A

IMU 3DM-GX3 -25 datasheet

LORD PRODUCT DATASHEET

3DM-GX3® -25

Miniature Attitude Heading Reference System

The **3DM-GX3®** -25 is a high-performance, miniature Attitude Heading Reference System (AHRS), utilizing MEMS sensor technology. It combines a triaxial accelerometer, triaxial gyro, triaxial magnetometer, temperature sensors, and an on-board processor running a sophisticated sensor fusion algorithm to provide static and dynamic orientation, and inertial measurements.

Features & Benefits

Best in Class

- precise attitude estimations
- high-speed sample rate & flexible data outputs
- high performance under vibration and high *g*

Easiest to Use

- smallest, lightest industrial AHRS available
- simple integration supported by SDK and comprehensive API

Cost Effective

- reduced cost and rapid time to market for customer's applications
- aggressive volume discount schedule

Applications

Accurate guidance, orientation and positioning under dynamic conditions such as:

- Inertial Aiding of GPS
- Unmanned Vehicle Navigation
- Platform Stabilization, Artificial Horizon
- Antenna and Camera Pointing
- Health and Usage Monitoring of Vehicles
- Reconnaissance, Surveillance, and Target Acquisition
- Robotic Control
- Personnel Tracking

System Overview

The **3DM-GX3®** -25 offers a range of fully calibrated inertial measurements including acceleration, angular rate, magnetic field, deltaTheta and deltaVelocity vectors. It can also output computed orientation estimates including Euler angles (pitch, roll, and heading (yaw)), rotation matrix and quaternion. All quantities are fully temperature compensated and are mathematically aligned to an orthogonal coordinate system. The angular rate quantities are further corrected for g-sensitivity and scale factor non-linearity to third order. The 3DM-GX3® -25 architecture has been carefully designed to substantially eliminate common sources of error such as hysteresis induced by temperature changes and sensitivity to supply voltage variations. Gyro drift is eliminated in AHRS mode by referencing magnetic North and Earth's gravity and compensating for gyro bias. On-board coning and sculling compensation allows for use of lower data output rates while maintaining performance of a fast internal sampling rate. For those users, integrators or OEMs who develop their own orientation and navigation applications, the 3DM-GX3® -25 is shipped with a complete Data Communications Protocol guide that provides access to the powerful LORD MicroStrain® Inertial Packet Protocol (MIP). Applications of your own design can readily be developed in any coding language and on any computing platform including microprocessors. The 3DM-GX3® -25 is initially sold as a starter kit consisting of an AHRS+GPS module, RS-232 or USB communication and power cable, software CD, user manual and quick start guide.

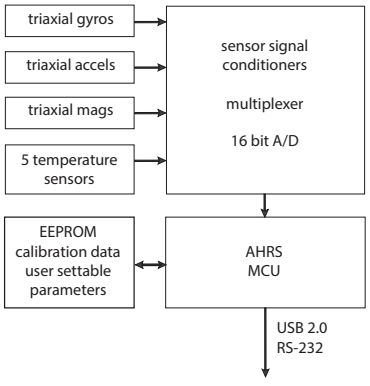

best of sensors expo 2009
Silver Level Winner

LORD MicroStrain®
SENSING SYSTEMS

Specifications

AHRS Specifications

Attitude and Heading	
Attitude heading range	360° about all 3 axes
Accelerometer range	±5*g* standard
Gyroscope range	±300°/sec standard
Static accuracy	±0.5° pitch, roll, heading typical for static test conditions
Dynamic accuracy	±2.0° pitch, roll, heading for dynamic (cyclic) test conditions and for arbitrary angles
Long term drift	eliminated by complimentary filter architecture
Repeatability	0.2°
Resolution	<0.1°
Data output rate	up to 1000 Hz
Filtering	sensors sampled at 30 kHz, digitally filtered (user adjustable) and scaled into physical units; coning and sculling integrals computed at 1 kHz
Output modes	acceleration, angular rate, and magnetic field deltaTheta, deltaVelocity, Euler angles, quaternion, rotation matrix
General	
A/D resolution	16 bits SAR oversampled to 17 bits
Interface options	USB 2.0 or RS232
Baud rate	115,200 bps to 921,600 bps
Power supply voltage	+3.2 to +16 volts DC
Power consumption	80 mA @ 5 volts with USB
Connector	micro-DB9
Operating temperature	-40° C to +70° C
Dimensions	44 mm x 24 mm x 11 mm - excluding mounting tabs, width across tabs 37 mm
Weight	18 grams
ROHS	compliant
Shock limit	500 *g*
Software utility	CD in starter kit (XP/Vista/Win7/Win8 compatible)
Software development kit (SDK)	complete data communications protocol and sample code

Senror Specifications

	Accels	Gyros	Mags
Measurement range	±5 *g*	±300°/sec	±2.5 Gauss
Non-linearity	±0.1 % fs	±0.03 % fs	±0.4 % fs
In-run bias stability	±0.04 m*g*	18°/hr	—
Initial bias error	±0.002 *g*	±0.25°/sec	±0.003 Gauss
Scale factor stability	±0.05 %	±0.05 %	±0.1 %
Noise density	80 µ*g*/√Hz	0.03°/sec/√Hz	100 µGauss/√Hz
Alignment error	±0.05°	±0.05°	±0.05°
User adjustable bandwidth	225 Hz max	440 Hz max	230 Hz max
Sampling rate	30 kHz	30 kHz	7.5 kHz max
Options			
Accelerometer range	±1.7 *g*, ±16 *g*, ±50 *g*		
Gyroscope range	±50°/sec, ±600°/sec, ±1200°/sec		

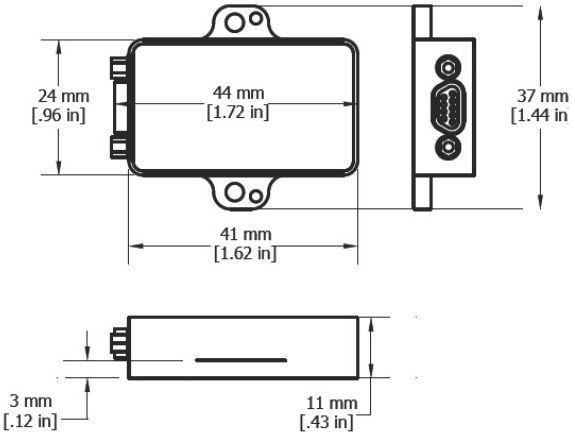

8400-0033 rev. 003

LORD Corporation
MicroStrain® Sensing Systems
459 Hurricane Lane,
Suite 102
Williston, VT 05495 USA
www.microstrain.com
ph: 800-449-3878
fax: 802-863-4093
sales@microstrain.com
Patent Pending

Appendix B

Matlab code

Main.m

```
1  global output_dir
2  save_figures=true;
3  filename='../data/GyroData_23_10_2015_15_52_34_test4.txt'; gyro_units =
       'rad/s'; acc_units='g';
4  data_range=2*10^5:6.32*10^5; %remove initial and final perturbations
5  header_lines=6;
6  [f1,file_base_name] = fileparts(filename);
7  output_dir=['results_',file_base_name];
8  mkdir(output_dir);
9  output_dir=[output_dir,filesep];
10 test_import=importdata(filename,',',header_lines);   %Read data txt;
       separated by comma; 6 header lines;
11 dataVector=test_import.data;
12 if ~exist('data_range','var')
13     data_range=1:length(dataVector(:,1));
14 end
15 XYZ_Aceler(:,1)=dataVector(data_range,1);
16 XYZ_Aceler(:,2)=dataVector(data_range,2);
17 XYZ_Aceler(:,3)=dataVector(data_range,3);
18 XYZ_Gyro(:,1)=dataVector(data_range,4);
19 XYZ_Gyro(:,2)=dataVector(data_range,5);
20 XYZ_Gyro(:,3)=dataVector(data_range,6);
21 time_stamp(:,1)=dataVector(:,7);
22 %% Convert units
23 if strcmp(gyro_units,'rad')
24     XYZ_Gyro=XYZ_Gyro*180/pi;  %rad to deg
25     gyro_units = 'degrees/s';
26 end
27 if strcmp(acc_units,'g')
28     XYZ_Aceler=XYZ_Aceler*9.8;  %g to m/s
```

```
29      acc_units = 'm/s^2';
30  end
31  %% Pre-process data
32  [XYZ_Gyro_processed,time_vector,sampling_frequency]=preprocess(XYZ_Gyro
        ,time_stamp,'Gyroscope',save_figures);
33  [XYZ_Aceler_processed,time_vector,sampling_frequency]=preprocess(
        XYZ_Aceler,time_stamp,'Accelerometer',save_figures);
34  %% Noise analysis
35  pts=100;
36  gyro_allan_coefficients = noise_analysis(XYZ_Gyro_processed,time_vector
        ,sampling_frequency,pts,'Gyroscope Allan variance','degrees/s',
        save_figures);
37  accel_allan_coefficients = noise_analysis(XYZ_Aceler_processed,
        time_vector,sampling_frequency,pts,'Accelerometer Allan variance','m
        /s^2',save_figures);
38  %% Denoising
39  wavelet_decomp_level=12;
40  median_filter_n = 20;%round(1.5/(1/sampling_frequency));
41  [XYZ_Gyro_filter_denoised,XYZ_Gyro_wavelet_denoised,
        XYZ_Gyro_KF_denoised] = denoising(XYZ_Gyro_processed,1/
        sampling_frequency,median_filter_n,wavelet_decomp_level);
42  %filter initial median peak
43  XYZ_Gyro_filter_denoised = XYZ_Gyro_filter_denoised(3:end,:);
44  [XYZ_Aceler_filter_denoised,XYZ_Aceler_wavelet_denoised,
        XYZ_Aceler_KF_denoised] = denoising(XYZ_Aceler_processed,1/
        sampling_frequency,median_filter_n,wavelet_decomp_level);
45  %filter initial peaks
46  XYZ_Aceler_filter_denoised = XYZ_Aceler_filter_denoised(3:end,:);
47  %% Post Noise analysis
48  pts=100;
49  gyro_allan_coefficients_denoised = noise_analysis(
        XYZ_Gyro_filter_denoised,time_vector,sampling_frequency,pts,'
        Gyroscope (filtered) Allan variance','degrees/s',save_figures,
        xlim_gyro,ylim_gyro);
50  accel_allan_coefficients_denoised = noise_analysis(
        XYZ_Aceler_filter_denoised,time_vector,sampling_frequency,pts,'
        Accelerometer (filtered) Allan variance','m/s^2',save_figures,
        xlim_acc,ylim_acc);
51  save_allan_results(gyro_allan_coefficients,
        gyro_allan_coefficients_denoised,'Gyroscope_allan_results');
52  save_allan_results(accel_allan_coefficients,
        accel_allan_coefficients_denoised,'Accelerometer_allan_results');
53  gyro_allan_coefficients_wavelet_denoised = noise_analysis(
        XYZ_Gyro_wavelet_denoised,time_vector,sampling_frequency,pts,'
        Gyroscope (wavelet) Allan variance','degrees/s',save_figures,
        xlim_gyro,ylim_gyro);
54  accel_allan_coefficients_wavelet_denoised = noise_analysis(
```

```
    XYZ_Aceler_wavelet_denoised,time_vector,sampling_frequency,pts,'
    Accelerometer (wavelet) Allan variance','m/s^2',save_figures,
    xlim_acc,ylim_acc);
```

noise analysis.m

```
function results=noise_analysis(data,time_vector,sampling_frequency,pts
    ,title_label,units,save_figures,xlim_values,ylim_values)
disp('*******************************************');
disp([mfilename, ' started']);
error_tolerated=0.15;
error_bias_tolerated=0.1;
results=zeros(5,3);
seconds_duration = time_vector(end) - time_vector(1);
[retval,tau,m1,fs,t0]=allan_leslie(data,seconds_duration,30);
tau_log = log10(tau);
retval_log = log10(retval);
slopes=[];
for i=1:length(retval_log)-1
    slopes(i,:)=(retval_log(i+1,:)-retval_log(i,:))/(tau_log(i+1)-
        tau_log(i));
end
labels = ['X','Y','Z'];
for i=1:3
    disp('-----------------------------------------');
    disp(['Axis analysis ',labels(i)]);
    %Random walk noise
    tau1=find(abs(tau-1)==min(abs(tau-1)));
    random_walk_noise_exist = slopes(tau1-1,i)-(-0.5)<=error_tolerated;
    if random_walk_noise_exist==1
        random_walk_noise = (retval(tau1,i)*60.0);
        results(1,i) = random_walk_noise;
        disp(['Random walk noise:',num2str(round_decimals(
            random_walk_noise,3))]);
    else
        results(1,i) = nan;
        disp('Random walk noise does not exist')
    end
    %rate ramp slope=1 tau=sqrt(2)
    tau2_first=find(tau<sqrt(2),1,'last');
    tau2=find(tau>sqrt(2),1);
    pendiente=(retval_log(tau2,i)-retval_log(tau2_first,i))/(tau_log(
        tau2)-tau_log(tau2_first));
    b = retval_log(tau2_first,i)-pendiente*tau_log(tau2_first); % y=
        pendiente*x+b
    if abs(pendiente-(1))<error_tolerated
        sigma_sqrt2=(pendiente*sqrt(2)+b)*60.0; %retval for sqrt(2)
```

```
37          disp(['Rate ramp noise:',num2str(round_decimals(sigma_sqrt2,3))
                ]);
38          results(2,i)=sigma_sqrt2;
39      else
40          disp('Rate ramp noise does not exist')
41          results(2,i)=nan;
42      end
43      %quantization noise slope=-1 tau=sqrt(3)
44      if abs(pendiente-(-1))<error_tolerated
45          sigma_sqrt3=(pendiente*sqrt(3)+b)*60.0; %retval for sqrt(3)
46          disp(['Quantization noise:',num2str(round_decimals(sigma_sqrt3
                ,3))]);
47          results(3,i) = sigma_sqrt3;
48      else
49          disp('Quantization noise does not exist')
50          results(3,i) = nan;
51      end
52      %rate random walk slope=0.5 tau=3
53      tau3_first=find(tau<3,1,'last');
54      tau3_end=find(tau>3,1);
55      pendiente=(retval_log(tau3_end,i)-retval_log(tau3_first,i))/(
            tau_log(tau3_end)-tau_log(tau3_first));
56      b = retval_log(tau3_end,i)-pendiente*tau_log(tau3_end);
57      if abs(pendiente-(0.5))<error_tolerated
58          sigma_3=(pendiente*3+b)*60.0; %retval for 3
59          disp(['Rate random walk noise:',num2str(sigma_3)]);
60          results(4,i) = sigma_3;
61      else
62          disp('Rate random walk noise does not exist')
63          results(4,i) = nan;
64      end
65      %bias instability
66      idx_slope0 = abs(slopes(:,i))<error_bias_tolerated;
67      bias_instability=(min(retval(idx_slope0,i))/0.644)*3600;
68      %bias_instability=(min(retval(:,i))/0.644)*3600;
69      if ~isempty(bias_instability)
70          disp(['Bias instability:',num2str(round_decimals(
                bias_instability,3)),' dps/h']);
71      else
72          bias_instability=nan;
73          disp('Bias instability does not exist');
74      end
75      results(5,i) = bias_instability;
76  end
77  disp([mfilename, ' finished']);
78  disp('*******************************************');
79  end
```

allan leslie.m

```
function [sigma,T,m1,fs,t0]=allan_leslie(XYZ_vector,seconds,pts)
 [N,M] = size(XYZ_vector);
 fs= ceil(N/seconds);  % sampling frequency in Hertz
 n = 2.^(0:floor(log2((N-1)/2)))'; % determine largest bin size
 maxN = n(end);
 endLogInc = log10(maxN);
 m = unique(ceil(logspace(0,endLogInc,pts)))'; % create log spaced
     vector average factor
 m1 = unique(ceil(logspace(0,endLogInc,pts)))'; %test
 t0 = 1/fs; % t0 = sample interval   the sample period
 T = m*t0;  % T = length of time for each cluster
 sigma2 = zeros(length(T),M); % array of dimensions (cluster periods) X
     (#variables)
 for j=1:M
     theta(:,j) = cumsum(XYZ_vector(:,j))*t0;  % integration of samples
         over time to obtain output angle ?
     for i=1:length(m)  % loop over the various cluster sizes
       for k=1:N-2*m(i) % implements the summation in the AV equation
           sigma2(i,j) = sigma2(i,j) + (theta(k+2*m(i),j) - 2*theta(k+
              m(i),j) + theta(k,j)).^2;
       end
     end
      sigma22(:,j) = sigma2(:,j)./repmat((2*T.^2.*(N-2*m)),1,1);
      sigma(:,j) = sqrt(sigma22(:,j));
 end
 end
```

remove outliers.m

```
function data=remove_outliers(data,title_label,save_figures)
global output_dir
iqr_data=iqr(data);
quartile1=quantile(data,0.25);
quartile3=quantile(data,0.75);
lower_bound=quartile1-3*iqr_data;
upper_bound=quartile3+3*iqr_data;
figure;
plot(data);
title(title_label);
hline = refline([0 lower_bound]);
hline.Color = 'r';
hline2 = refline([0 upper_bound]);
hline2.Color = 'r';
legend('raw data','+-3*IQR boundaries','Location','best')
%detect them
```

```
idx_outliers_upper=data>upper_bound;
idx_outliers_lower=data<lower_bound;
%remove them
data(idx_outliers_upper|idx_outliers_lower)=median(data);
 if save_figures
     savefig([output_dir,title_label,'.fig'])
     print([output_dir,title_label,'.eps'],'-depsc')
     print([output_dir,title_label,'.png'],'-dpng')
 end
end
```

preprocess.m

```
function [data,time_vector,sampling_frequency]=preprocess(data,
    time_vector,title_label,save_figures)
disp('*****************************************');
disp([mfilename, ' started']);
%Remove outliers
data(:,1)=remove_outliers(data(:,1),[title_label,' X axis'],
    save_figures);
data(:,2)=remove_outliers(data(:,2),[title_label,' Y axis'],
    save_figures);
data(:,3)=remove_outliers(data(:,3),[title_label,' Z axis'],
    save_figures);
%Regularize time sampling
%Identify sampling time and frequency
nanoseconds= time_vector(end)- time_vector(1); % time in nanoseconds of
     the hole data set
seconds= nanoseconds/10^9; % conversion seconds
nHours=seconds/3600;  % hours for if it is neccesary and to have idea
time_stamp_seconds=(time_vector-time_vector(1))/1e9;
diff_time_stamp=diff(time_stamp_seconds);
%histogram of sampling times with width=min(sampling times)
%histograma=histc(diff_time_stamp,0:min(diff_time_stamp):max(
    diff_time_stamp)+1);
sampling_time=round(median(diff_time_stamp)*1000)/1000;%floor(find(
    histograma==max(histograma))*min(diff_time_stamp)*100)/100;
sampling_frequency=1/sampling_time;
time_vector=0:sampling_time:sampling_time*(length(data(:,1))-1);
disp([mfilename, ' finished']);
disp('*****************************************');
end
```

denoising.m

```
% Denoising
function [filt_data_denoised,wavelet_data_denoised,kf_dat_denoised] =
```

```
    denoising(data_vector,sampling_time,median_filter_n,
    wavelet_decomp_level)
disp('*******************************************');
disp([mfilename, ' started']);
[m,n] = size(data_vector);
sampling_frequency = 1/sampling_time;
for i=1:n
    data = data_vector(:,i);
    %% Filtering
    filt_data_denoised(:,i)=medfilt1(data,median_filter_n);
    %% Fast fourier transform
    fft_values = fft(data);
    L=length(data);
    %Compute the two-sided spectrum P2. Then compute the single-sided
       spectrum P1 based on P2 and the even-valued signal length L.
    P2 = abs(fft_values/L);
    P1 = P2(1:L/2+1);
    P1(2:end-1) = 2*P1(2:end-1);
    %Define the frequency domain f and plot the single-sided amplitude
       spectrum P1.
    %The amplitudes are not exactly at 0.7 and 1, as expected, because
       of the added noise.
    %On average, longer signals produce better frequency approximations
       .
    f = sampling_frequency*(0:(L/2))/L;
    figure;
    plot(f,P1)
    title('Single-Sided Amplitude Spectrum of X(t)')
    xlabel('f (Hz)')
    ylabel('|P1(f)|')
    %Get the mean value and calculate a threshold:
    mean_value = mean(abs(fft_values));
    threshold  = 1.1*mean_value; % Fine-tune this
    %Remove everything that's below the threshold (we assume that it
       corresponds to noise):
    fft_values = fft(data);
    %Remove everything that's below the threshold (we assume that it
       corresponds to noise):
    fft_values(abs(fft_values) < threshold) = 0;
    %Get the filtered data:
    fft_data_denoised(:,i) = ifft(fft_values);
    %% Wavelet decomposition.
    [c,l] = wavedec(data,wavelet_decomp_level,'sym8');
    % threshold the decomposition structure [c,l].
    wavelet_data_denoised(:,i) = wden(c,l,'minimaxi','s','sln',
       wavelet_decomp_level,'sym8');
  end
```

```
41 disp([mfilename, ' finished']);
42 disp('********************************************');
43 end
```

plot allan variance.m

```
1  function plot_allan_variance(sigma,T,title_label,units,save_figures,
       xlim_values,ylim_values,allan_values)
2  global output_dir
3  ind=find(title_label==' ');
4  main_label = title_label(1:ind(1)-1);
5  x=sigma(:,1);
6  y=sigma(:,2);
7  z=sigma(:,3);
8  figure;
9  loglog(T,x,'b','LineWidth',2);
10 title(title_label);
11 hold on;
12 loglog(T,y,'g','LineWidth',2);
13 loglog(T,z,'r','LineWidth',2);
14 legend([main_label,' X'],[main_label,' Y'],[main_label,' Z']);
15 xlabel('\tau (secs)');
16 ylabel(['\sigma (',units,')'])
17 set(gca,'XMinorGrid','On');
18 set(gca,'XGrid','On');
19 set(gca,'YMinorGrid','On');
20 set(gca,'YGrid','On');
21 set(gca,'MinorGridAlpha',0.95)
22 % plot lines with m=-0-5 for random walk noise
23 lx=log10(x);
24 ly=log10(y);
25 lz=log10(z);
26 lt=log10(T);
27 xo=find(abs(lt)<0.1,1);
28 bx=lx(xo)-0.5*lt(xo);
29 by=ly(xo)-0.5*lt(xo);
30 bz=lz(xo)-0.5*lt(xo);
31 yxfit=-0.5*lt+bx;
32 yyfit=-0.5*lt+by;
33 yzfit=-0.5*lt+bz;
34 loglog(T,10.^yxfit,'b--');
35 loglog(T,10.^yyfit,'g--');
36 loglog(T,10.^yzfit,'r--');
37 if ~isempty(xlim_values) && ~isempty(ylim_values)
38     ylim_current_values=get(gca,'YLim');
39     ylim_values = [min(ylim_current_values(1),ylim_values(1)), max(
          ylim_current_values(2),ylim_values(2))];
```

```
40      xlim(xlim_values);
41      ylim(ylim_values);
42  else
43      xlim([10^round(min(lt)),10^ceil(max(lt))]);
44      ylim([10^floor(min([lx;ly;lz])),10^ceil(max([lx;ly;lz]))]);
45  end
46  % plot red dotted vertical line in tau=10^0
47  SP=1;
48  line([SP SP],get(gca,'YLim'),'Color',[1 0 0],'LineStyle','--')
49  if strcmp(main_label,'Gyroscope')
50      noise_labels={'ARW','RR','QN','RRW','BI'};
51  else
52      noise_labels={'VRW','RR','QN','RRW','BI'};
53  end
54  for i=1:5
55      if ~all(isnan(allan_values(i,:)))
56          t = annotation('textbox');
57          t.String = sprintf('%s X:%.3f\n%s Y:%.3f\n%s Z:%.3f',
                noise_labels{i},allan_values(i,1),noise_labels{i},
                allan_values(i,2),noise_labels{i},allan_values(i,3));
58          t_pos = t.Position;
59          t_pos(1) = 0.5;
60          t_pos(2) = 0.5;
61          t.Position = t_pos;
62      end
63  end
64  if save_figures
65      savefig([output_dir,title_label,'.fig'])
66      print([output_dir,title_label,'.eps'],'-depsc')
67      print([output_dir,title_label,'.png'],'-dpng')
68  end
69  end
```

save allan results.m

```
1  function save_allan_results(allan_coef,allan_coef_denoised,title_file)
2  global output_dir
3  [m,n] = size(allan_coef);
4  fileID = fopen([output_dir,title_file,'.csv'],'w','n','ISO-8859-1');
5  fprintf(fileID,',X,Y,Z,X (denoised),Y (denoised),Z (denoised)\n');
6  noise_labels={'Random walk','Rate ramp','Quantization noise','Rate
       random walk','Bias instability'};
7  for i=1:m
8      noise_label=noise_labels{i};
9      fprintf(fileID,'%s,%f,%f,%f,%f,%f,%f\n',noise_label,allan_coef(i,1)
           ,allan_coef(i,2),allan_coef(i,3),allan_coef_denoised(i,1),
           allan_coef_denoised(i,2),allan_coef_denoised(i,3));
```

```
10 end
11 fclose(fileID);
```

Acronyms

INS	Inertial Navigation System
IMU	Inertial Measurement Unit
MEMS	Micro Electromechanical Systems
NMR	Nuclear Magnetic Resonance
FOG	Fiber Optic Gyro
RLG	Ring Lasers Gyro
IFOG	Interferometric Fiber Optic Gyro
RFOG	Resonant Fiber Optic Gyro
PCF	Photonic Crystal Fiber
MOG	Micro Optic Gyro
CCID	Charge Coupled Imaging Device
MOEMS	Micro-Opto Electromechanical Systems
BRW	Bias Random Walk
PSD	Power Spectral Density
ARW	Angle Random Walk
VRW	Velocity Random Walk
FFT	Fast Fourier Transform
IEEE	Institute of Electrical and Electronic Engineers
AVAR	Allan Variance
RMS	Root Means Square
RAVAR	Root Allan Variance
DWT	Discrete Wavelet Transform
CWT	Continous Wavelet Transform
LOD	Level of Decomposition
AHRS	Attitude Heading Reference System
IQR	Interquartile Range
pdf	probability density function